8-2022

Digital and Gradient Refractive Index Planar Optics by Nanoimprinting Porous Silicon

Anna Hardison
hardis3@clemson.edu

DIGITAL AND GRADIENT REFRACTIVE INDEX PLANAR OPTICS BY NANOIMPRINTING POROUS SILICON

A Thesis
Presented to
The Graduate School of
Clemson University

In Partial Fulfillment
of the Requirements for the Degree
Master of Science
Electrical Engineering

By Anna Hardison
August 2022

Committee Members:
Dr. Judson D. Ryckman, Committee Chair
Dr. William R. Harrell
Dr. Apoorva Kapadia

ABSTRACT

Due to the drawbacks of traditional refractive optics, the implementation of planar or nearly planar optical devices has been of research interest for over a century. Subwavelength gratings are a particularly promising option for creating flat optical devices; however, the implementation of subwavelength grating-based optics is limited by fabrication constraints. Recently, we implemented flat optical devices using the nanoimprinting of refractive index (NIRI) process, a process which was pioneered in a previous study but remained largely unproven in terms of device fabrication. The planar, gradient index microlenses we fabricated were found to possess an effective medium similar to a subwavelength grating. We determined that the gradient index planar microlenses successfully focused collimated incident light with focal full-width-half-maximums of less than 14 μm at wavelengths as low as 406 nm. We also fabricated digitally patterned waveguides between 0.35 and 2 μm in width using the NIRI process. We found a propagation loss in the non-oxidized waveguides of 8.1 ± 0.245 dBm/mm, which we were able to reduce by roughly 8 times following a full oxidation of the waveguides.

DEDICATION

To my parents and my sister

ACKNOWLEDGEMENTS

I am deeply indebted to my graduate research professor and committee chair Dr. Judson Ryckman for his guidance, input, and collaboration throughout the course of my research. I am also grateful to my other committee members Dr. Apoorva Kapadia and Dr. William Harrell for their support. The completion of my thesis also would not have been possible without the valuable insight and contributions of my former colleague, Dr. Tahmid Talukdar, a pioneer of the Nanoimprinting of Refractive Index process. He not only introduced me to the NIRI process and lab procedures, but also contributed microlens simulation work to this project. I am also grateful to Dr. Ivan Kravchenko of Oak Ridge National Laboratories, another contributor to this project who fabricated the waveguide stamps and provided a detailed description of his process. I would like to thank my other colleagues for their support as well as their insight and constructive criticism expressed during our weekly research group meetings. I would also like to express my gratitude to my family and friends for their support over the course of my research and writing process.

TABLE OF CONTENTS

Page

LIST OF FIGURES

CHAPTER 1

SURVEY OF FLAT OPTICS

Currently, most optics applications are dominated by conventional, bulk refractive optical devices. True to their name, refractive optics rely on refraction to modify incident wavefronts. The two parameters used to shape the output wavefront are the bulk refractive index and geometry of the device [1]. Most refractive optics are created using high temperature silica or quartz fusion processes followed by molding, which requires precise shaping and polishing of the surface [2], [3]. In addition to their involved fabrication, refractive optics tend to be relatively bulky and heavy. This is particularly true in applications where a high resolution is required, as there is an inherent trade-off in refractive optics between thickness and numerical aperture, as shown in Figure 1 A [4]. There is an increased need for small, lightweight optical devices due to the general technological trends towards miniaturization and integration as well as some novel applications such as LiDAR and virtual reality [2].

Flat optics can perform the same operations as refractive optics but are significantly thinner and less bulky. By definition, flat optics have thicknesses on the order of or less than the incident wavelength [1]. The earliest flat optics were diffractive optics, where the wavelength-scale thickness of the optics cause diffraction to dominate over refraction [1]. The earliest example of a flat, diffractive optical device was the Fresnel Zone Plate, invented in 1866 [5]. In a flat, diffractive optical device, various regions of the flat device surface are patterned or modified in some way to shift the phase of the incident light. In a flat diffractive lens, the phases of the various regions of the lens are designed such that the output light interferes constructively at the focal point [4]. Over the past century, fabrication techniques have improved in precision, allowing for the

fabrication of flat optics with deeply subwavelength features. In this deeply subwavelength regime, conventional diffraction theory doesn't sufficiently describe the behavior of the flat optical devices. The deeply subwavelength structures can either behave as an effective homogenous medium, as in a subwavelength grating [6], or shape the incident wavefront through resonance, as in a metasurface [7]. This chapter will discuss diffractive optics, metasurfaces, and subwavelength gratings, with a particular emphasis on the latter.

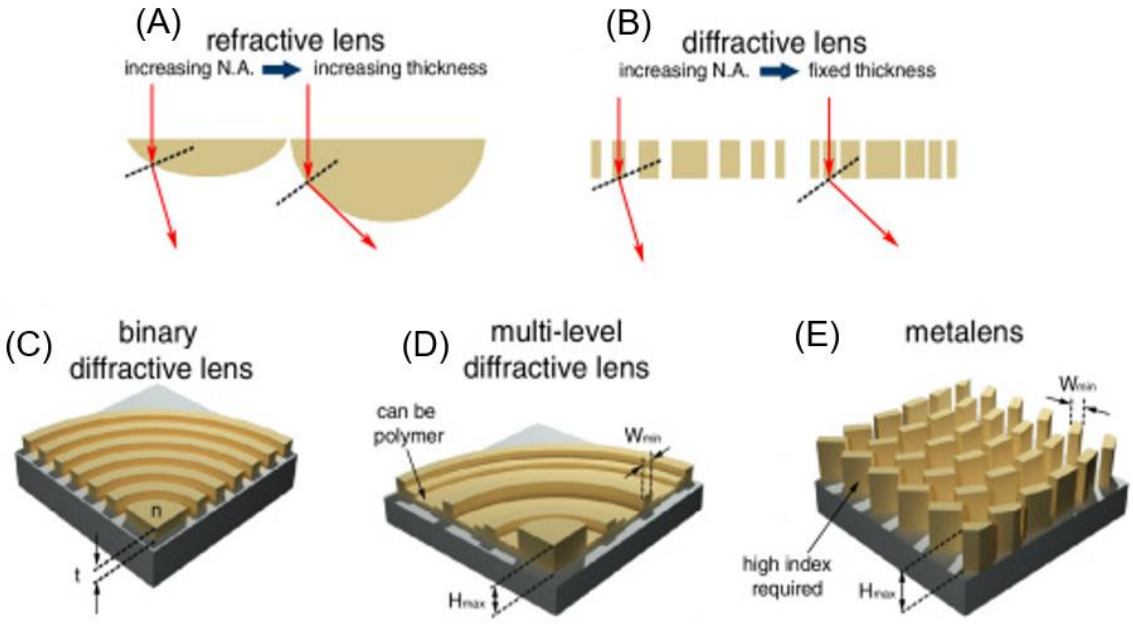

Figure 1. (A) numerical aperture vs thickness of refractive optics [4] (B) numerical aperture of diffractive lenses depends on period, not thickness [4] (C) model of a binary diffractive lens (not to scale) [4] (D) model of a multi-level diffractive lens (not to scale)[4] (E) model of a high index metalens (not to scale) [4]

1.1 Diffractive Optics

When they were first introduced, diffractive optics held a significant advantage over refractive optics in terms of spatial profile. Subsequent innovations in diffractive optics increased the optical efficiency of diffractive systems from the relatively low 10% efficiency of the Fresnel zone plate, making diffractive optics more useful in a wider variety of applications [8]. In modern optics, diffractive optical devices can be categorized into two categories based on their basic constituent

topologies. These are binary diffractive optics and multilevel diffractive optics. Binary diffractive optical elements consist of arrays of uniform thickness, wavelength-scale elements arranged periodically. In the case of a circular binary diffractive lens, these elements are typically arranged in concentric circles around the center, as shown in Figure 1 C. The phase shift of a specific location on a binary diffractive device is controlled by the local period between the binary diffractive elements, as shown in Figure 1 B [4]. In a circular lens, each point along the radius r has a different distance from the focal point located above the center of the lens, so each radial point in a binary diffractive lens must shift the phase of the incident light to correspond to the local path length. Because of this principle, the period between the binary diffractive elements decreases towards the edges of the lens. Generally, the local period in a binary diffractive lens is designed according to the following equation:

$$r_m = 2mf\lambda_0 + (m\lambda_0)^2 \quad (1)$$

Here, r_m is the radius of the m_{th} period, f is the overall focal length of the lens, and λ_0 is the incident wavelength. The width of the m_{th} period of the lens is defined as $r_m - r_{m-1}$ [9]. The range of achievable phase shifts in a binary diffractive optic depends on the thickness of the binary diffractive elements. In order to get a full 2π phase shift, the thickness t of the binary elements must be at least $\lambda/(n-1)$ [4].

A persistent issue with binary diffractive optical devices is their limited focusing efficiency, particularly at broadband, as well as chromatic aberration [10]. To address these issues, a second type of diffractive optical device was developed, known as blazed or multilevel diffractive optical devices. As their name suggests, the diffractive elements can take on a range of discretized heights rather than only one as in binary diffractive optics [4]. The multilevel nature of multilevel diffractive optics allows for many more degrees of freedom, enabling for more flexible design and

better performance. Theoretically, multilevel diffractive optics can achieve a focusing efficiency of 100%, though this hasn't been observed in practice [11]. However, multilevel diffractive optical devices can still achieve much higher focusing efficiencies than their binary counterparts. There has also been a great deal of progress in making broadband multilevel diffractive optics. Early on, multilevel diffractive optics were designed to operate at multiple discrete wavelengths using higher diffraction orders, as in multiorder diffractive lenses [12], or by combining properties of diffractive and refractive optics, as in harmonic diffractive lenses [13]. Continuously broadband multilevel refractive optics have also been implemented more recently. For instance, N. Mohammed *et al*. demonstrated a multilevel diffractive lens with a focusing efficiency that exceeded 40% over a continuous band of 300 nm in the visible spectrum [14].

Multilevel diffractive optics can also be designed to severely limit chromatic aberration. Chromatic aberration in binary refractive optics occurs because diffraction angle is directly proportional to incident wavelength [15]. This causes the focal point to move farther away as wavelength increases in a binary diffractive lens. Chromatic aberration can be compensated for in multilevel diffractive optics thanks to the added degrees of freedom in multilevel diffractive optical design, as demonstrated by Wang, Mohammed, and Menon [10]. They created three cylindrical, achromatic multilevel diffractive lenses that focused at three wavelengths between 460 nm and 620 nm. Throughout the visible range, the best performing lens showed a lateral focal shift of 1.3 μm laterally and 25 μm axially. The average optical power was found to be around 25%, which is relatively high for achromatic lenses.

Because of their relatively large feature size relative to incident wavelength, it is easy to fabricate flat diffractive optical devices using mature lithography technology used in CMOS. Binary diffractive optics can be fabricated in a single etch or curing step while multilevel

diffractive optical devices are fabricated using either a single greyscale lithography step or multiple binary lithography and etch steps [4]. Diffractive optical devices can be made of polymers or dielectric materials, which adds flexibility to the fabrication processes. A promising method for mass production of multilevel diffractive optical devices involves creating a stamp or template device using greyscale lithography and then replicating it using imprint lithography of polymers [10].

1.2: Metamaterials

Metamaterials are artificially created materials consisting of resonant, deeply subwavelength elements, designed to produce a specific electromagnetic response [7], [16]. Metamaterials have generated a large amount of press over the past two decades due to their exotic properties. In 2000, D. R. Smith *et al.* demonstrated a metasurface with a negative permittivity and a negative permeability, a so-called "left-handed" medium [17]. Shortly after this, Shelby, Smith and Schultz demonstrated a metamaterial with a negative refractive index [18]. Generally, the term 'metamaterial' refers to a 3D artificial resonant material. A major downside of these 3D metamaterials is their high attenuation. This attenuation issue was minimized by creating similar artificial materials in 2D, a class of materials that came to be known as metafilms or metasurfaces, first demonstrated in 2011 [19], [20]. Metasurfaces have since shown utility in the field of flat optics, as they have wavelength-scale thicknesses and can exert strong control over the characteristics of incident light, namely phase, amplitude, polarization and interface dispersion [21].

Metasurfaces operate based on the phase response of their constituent scatterers, or "meta-atoms," which are deeply subwavelength structures that locally modify incident light. The phase discontinuity caused by the meta-atoms can be characterized using the generalized laws of

reflection and refraction. Considering a situation where a plane wave travelling through a medium with index n_i is incident on a metasurface with angle θ_i, and assuming a constant phase gradient over the metasurface, a generalized version of Snell's Law of refraction can be derived as follows:

$$\sin(\theta_t)\, n_t - \sin(\theta_i)\, n_i = \frac{\lambda_0}{2\pi}\frac{d\Phi}{dx} \quad (2)$$

Here, θ_t is the angle of refraction with respect to surface normal, and the quantities n_i and n_t are the refractive indices of the media above and below the metasurface respectively. The quantity λ_0 is the wavelength of the incident beam in a vacuum. The value Φ is the phase discontinuity encountered by the incident beam at a given point due to the meta-atoms at the interface, and *dx* is the distance along the interface. This means that the quantity $\frac{d\Phi}{dx}$ represents the gradient of phase discontinuity introduced by the meta-atoms along the metasurface [20]. A similar equation can be derived to describe the reflection at the metasurface interface:

$$\sin(\theta_r) - \sin(\theta_i) = \frac{\lambda_0}{2\pi n_i}\frac{d\Phi}{dx} \quad (3)$$

Where θ_r is the angle of reflection relative to surface normal. Unlike in traditional optics, the angles of reflection and refraction at the metalens interface do not have a linear relationship [20].

Early metasurfaces, known as plasmonic metasurfaces, operated using surface plasmon resonance in metallic meta-atoms. When each individual metal meta-atom is exposed to a time-varying electromagnetic field, such as incident light, the electrons in the meta-atom oscillate according to the Lorentzian oscillator model. This oscillation can be used to modify the phase of incident light. The exact surface plasmon resonance behavior of an individual oscillating meta-

atom depends on its physical geometry and material properties. Depending on the size of the meta-atom relative to the incident wavelength, the angle of the meta-atom relative to the incident field can also be a factor [22]. Angle-based phase modulation can be seen in the design of one of the earliest metasurfaces by Yu *et al.* that consists of an array of V-shaped meta-atom 'antennas', where the local phase and polarization responses were tailored by changing the angles of the two antenna arms, as shown in Figure 2 A [23]. A downside of these meta atoms was their low efficiencies, estimated to be 10 % under ideal circumstances.

There are further resonance phenomena associated with coupling between meta-atoms in a metasurface that can be tuned by changing the spacing between meta-atoms relative to their resonance wavelength. This resonance coupling can increase metasurface efficiency if harnessed effectively [22]. In order to fully capitalize on these resonance coupling phenomena, different types of meta-atoms and metasurface topologies needed to be designed [22]. The earliest example was the gap-plasmon metasurface, which used nanobrick-shaped metal meta-atoms deposited on top of an insulator substrate. The insulator substrate layer had another layer of metal beneath it, as shown in Figure 2 B [24]. These metasurfaces only worked in reflectance mode due to the presence of the reflective metal layer. To develop high-efficiency, transmission-mode metasurfaces, meta-atoms began to be fabricated from dielectric materials rather than metals. The earliest majority-dielectric metasurfaces were Huygens' metasurfaces [19]. Huygens' metasurfaces typically consist of an array of unit cells, each containing either a wire and a loop or three-layered, stacked planar metallic patterns sandwiched between dielectric layers, which is known as a cascaded topology. In some implementations the loop and wire are fabricated on different dielectric layers that are stacked on top of one another, while in others, both wire and loop are placed in the same plane [25]. An example device, a prism, created using Huygens'

metasurface with a cascaded topology can be seen in Figure 2 C [26]. Huygens' metasurfaces have extremely high transmission efficiencies at microwave and near-IR wavelengths, but relatively low transmission efficiency at visible wavelengths [19].

All dielectric metasurfaces with high efficiencies at visible wavelengths have been achieved using high index contrast dielectric materials. This category of metasurfaces is known as "high contrast metasurfaces," and is the type of metasurface pictured in Figure 1 E. The high-index materials in question tend to be those that are easily processed, such as silicon or germanium [27]. Each high contrast meta-atom acts as a tiny, truncated waveguide behaving like a Fabry-Perot oscillator. The high index contrast is needed for confinement in the meta-atoms, which maximizes the transmission efficiency of the metasurface [19]. The output light receives a polarization-dependent phase and polarization shift from the meta-atoms' oscillation. Similar to metallic meta-atoms, the polarization-dependent phase response of individual dielectric meta-atoms can be tuned by changing meta-atom geometry [27]. An example of a high-contrast metasurface topology can be seen in Figure 2 D, where local phase and polarization responses are tuned by adjusting the dimensions of the ellipse as well as its relative angle.

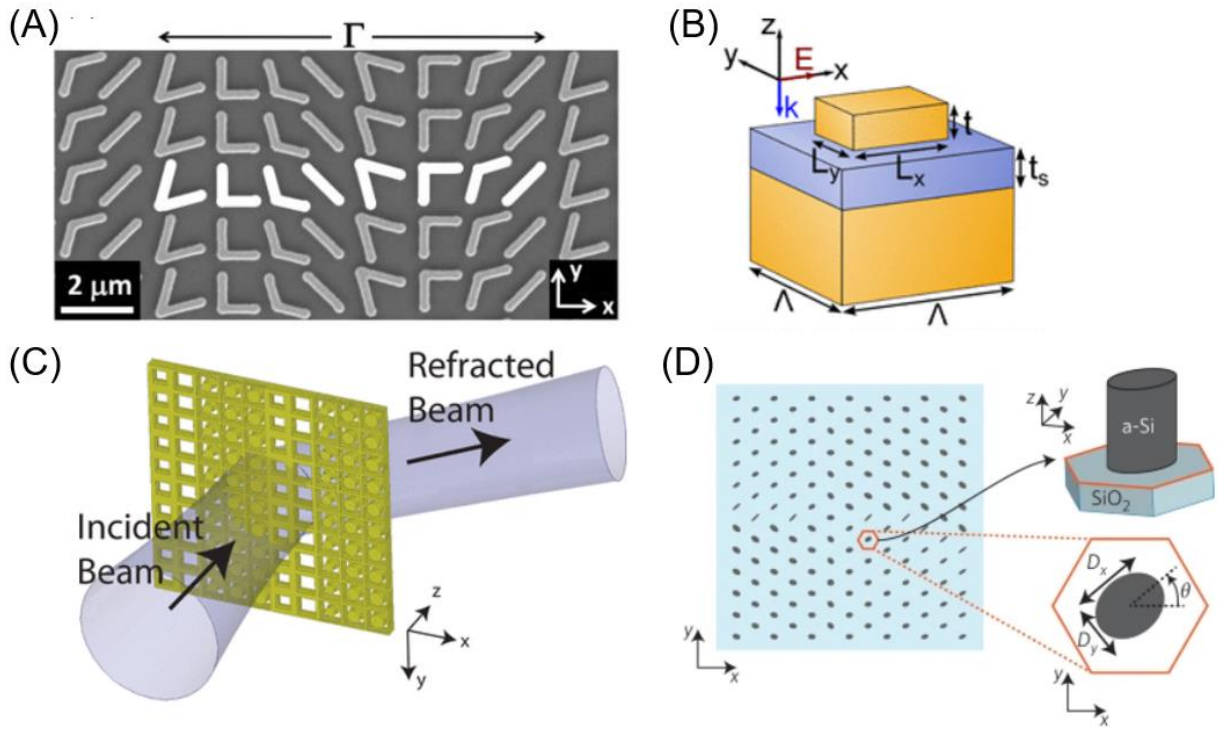

Figure 2. (A) A scanning electron microscope image of an early plasmonic metasurface made of gold deposited on silicon [23] (B) An example unit cell from a metal-insulator-metal plasmonic metasurface; the orange is gold, and the purple is silicon dioxide [24] (C) An example topology of a 3-layer Huygens' metalens designed to refract incident light at a given angle; each grid square is a unit cell created from a thin gold structure sandwiched between layers of SU-8 dielectric [26] (D) A high-contrast metasurface topology consisting of elliptical silicon columns arranged in a hexagonal grid on a silicon dioxide substrate [27]

A major limiting factor to the widespread commercialization of metasurfaces has been the difficulty of manufacturing them. For use in visible optics, feature sizes would need to be < 100 nm, below the limits of most traditional lithography techniques. Most metasurfaces fabricated in research settings are created using direct-write techniques such as electron-beam lithography [2]. However, direct write processes are too low throughput to be used in an industry setting. There is also ample research into alternative large-area lithography techniques such as maskless laser techniques, extreme-UV lithography and plasmonic lithography. These techniques have drawbacks in terms of the flexibility of the patterns they can create, as laser techniques can either create periodic or aperiodic structures (not both) and plasmonic lithography is limited to small

mask sizes, limiting throughput [19]. Some non-photolithographic methods such as nano-imprint lithography and self-assembly lithography have also been proposed but are still largely experimental. Self-assembly lithography is limited in the patterns it can create, but nano-imprint lithography has shown promise in terms of its high throughput, high resolution, and design flexibility. However, there are some issues with degradation of the imprinted polymer layer during the process [19].

1.3 Subwavelength Grating Principle of Operation

Subwavelength gratings are a type of metamaterial. Similar to the metasurfaces described in the previous section, subwavelength gratings are comprised of deeply subwavelength elements. However, unlike the metasurfaces described in the previous section, subwavelength gratings do not operate using resonance and are typically comprised of dielectric materials such as silicon [6]. Subwavelength gratings are notable in the fact that they are able to act like a homogenous, anisotropic material with effective refractive indices between that of the subwavelength structures and the surrounding medium. This effective refractive index can be adjusted by changing the local design of the grating. Subwavelength gratings have been of particular use in silicon photonics, where they have allowed for a wider range of refractive index profiles compared to binary-patterned silicon photonic components at typical length scales [28].

When a subwavelength grating is fashioned into a waveguide, as shown in Figure 3 A, it can be described by one of several different models depending on its period Λ as compared to the Bragg threshold: $\lambda_0/(2n_{eff})$. Here, λ_0 is the incident wavelength in a vacuum and n_{eff} is the effective index of the first Floquet-Bloch mode. When the period is less than the Bragg threshold, the subwavelength grating acts like a homogenous, anisotropic material described by a permittivity tensor:

$$\varepsilon = \begin{bmatrix} n_{xx}^2 & 0 & 0 \\ 0 & n_{yy}^2 & 0 \\ 0 & 0 & n_{zz}^2 \end{bmatrix}$$

(4)

Here, n_{xx}, n_{yy} and n_{zz} are the effective refractive indices in the x, y, and z directions respectively. These three effective indices are found through a process of homogenization, the specifics of which depend on how close the grating period is to the Bragg threshold. When the period of the subwavelength grating is much smaller than the Bragg threshold, an analytical method known as the laminar material model can be used [6]. As the name suggests, the subwavelength grating is modelled as a laminar periodic structure where each layer is transversally infinite, as shown in Figure 3 B. In this model structure, material 1 has thickness *a* and bulk refractive index n_1, and material 2 has thickness *b* and bulk refractive index n_2.

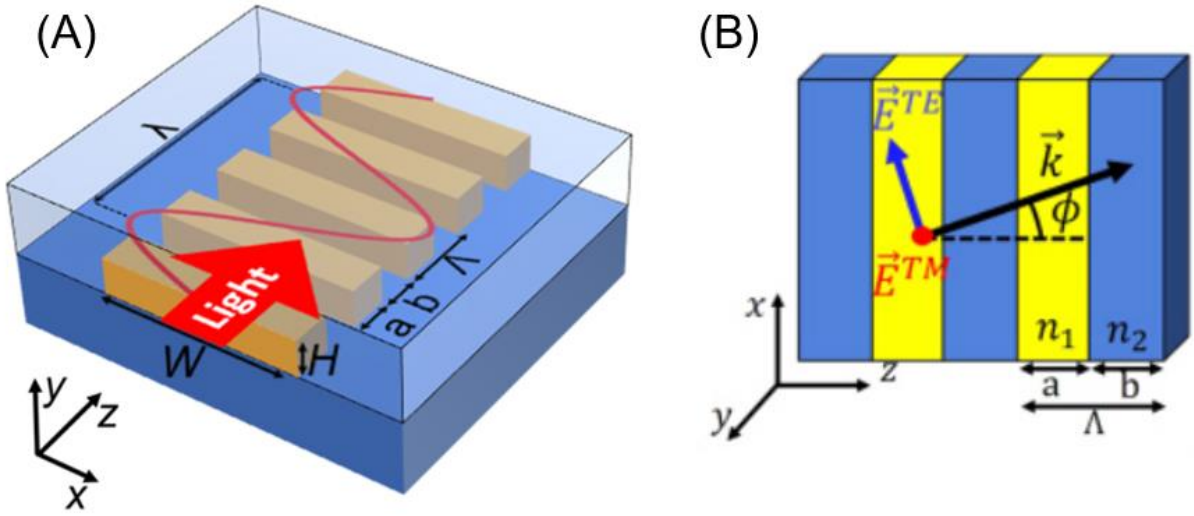

Figure 3. (A) a subwavelength grating waveguide [6] (B) a section of the laminar model structure [29]

It will be useful to examine a simple plane wave in the x-z direction using this model. This plane wave is described by the wave vector $\vec{k}(\varphi) = k_x\hat{x} + k_z\hat{z}$, where incidence angle $\varphi = \text{atan}\left(\frac{k_x}{k_z}\right)$. Propagation constants k_x and k_z are related by the following dispersion relation:

$$\cos(k_z \Lambda) = \cos(k_{1x} a)\cos(k_{2x} b) - \Delta \sin(k_{1x} a)\sin(k_{2x} b)$$

(5)

Here, $k_{ix} = \sqrt{\left(\frac{2\pi n_i}{\lambda_0}\right)^2 - {k_x}^2}$ where i = 1 or 2, and Δ depends on the polarization of the incident light. For TE and TM polarization, Δ can be found using the following two formulas:

$$\Delta_{TE} = \frac{1}{2}\left(\frac{n_2^2 k_{1x}}{n_1^2 k_{2x}} + \frac{n_1^2 k_{2x}}{n_2^2 k_{1x}}\right)$$

(6)

$$\Delta_{TM} = \frac{1}{2}\left(\frac{k_{1x}}{k_{2x}} + \frac{k_{2x}}{k_{1x}}\right)$$

(7)

Under the assumption of transversally infinite layers, and the assumption that $\lambda >> \Lambda$, the terms $k_z\Lambda << 1$, $k_z a << 1$, and $k_z b << 1$. This allows equations 5 through 7 to be simplified to the following form:

$$k_x^2 n_\perp^2 + k_z^2 n_\parallel^2 = k_0^2$$

(8)

$$k_x^2 n_\parallel^2 + k_z^2 n_\parallel^2 = k_0^2$$

(9)

Equations 8 and 9 describe the TE and TM polarizations respectively, where $n_{/\!/}$ and $n_\perp$ are the refractive indices of the equivalent material for polarization parallel ($n_{/\!/}$) and perpendicular ($n_\perp$) to the laminar layers [29], [30]. They can be solved for using the following two equations:

$$n_\parallel = \frac{k_z}{k_0}, \qquad k_x = 0$$

(10)

$$n_\perp = \frac{k_x}{k_0}, \qquad k_z = 0$$

(11)

The permittivity tensor representing the effective material can be approximated by the following:

$$\varepsilon_1 = \begin{bmatrix} n_{\parallel}^2 & 0 & 0 \\ 0 & n_{\parallel}^2 & 0 \\ 0 & 0 & n_{\perp}^2 \end{bmatrix}$$

(12)

The infinite laminar model simplifications can be easily applied to the subwavelength grating waveguide as pictured in Figure 3 A with a period much smaller than the Bragg threshold. The permittivity tensor for the waveguide can be simplified to equation 12, and the tensor components can be found using the following approximations:

$$n_{\parallel}^2 \approx \frac{a}{\Lambda} n_1^2 + \frac{b}{\Lambda} n_2^2$$

(13)

$$n_{\perp}^2 \approx \left(\frac{a}{\Lambda} n_1^{-2} + \frac{b}{\Lambda} n_2^{-2} \right)^{-1}$$

(14)

As is evident from these two formulas, the duty cycle of the grating has a significant effect on the polarization and effective refractive indices of the modes propagating through a subwavelength grating. If the duty cycle of the higher index material decreases, the effective index of the grating decreases. Because of this, duty cycle is one of the primary geometric parameters used to modify and implement photonic devices using subwavelength gratings [28].

As the period of the subwavelength grating approaches the Bragg threshold, the laminar model no longer accurately approximates its behavior. A different model must be used here, known as the slab material model. In this model, the subwavelength grating still behaves like a homogenous, birefringent material that can be described using a 3x3 diagonal permittivity tensor. However, the calculation of the permittivity tensor components cannot be done analytically as in the laminar model but must be solved numerically by simulation [6]. In addition to the parameters

used in the laminar model, the slab material model also accounts for the height of the subwavelength grating structures, labelled ‘H’ in Figure 3 A. When the period of the grating exceeds the Bragg threshold, scattering becomes significant and the structure can no longer be modelled as a homogenous material, but instead must be modelled like conventional photonic structures at wavelength scale.

1.4 Subwavelength Grating Applications

The refractive index patterning offered by subwavelength gratings has shown to be useful in a variety of applications, particularly in integrated silicon photonic circuits. Photonic devices such as waveguide couplers, photonic sensors, and fiber to chip couplers have shown significant enhancement with the addition of subwavelength grating elements. Subwavelength gratings also have the potential to be useful as flat optics, however it has been difficult to implement subwavelength grating optics due to fabrication difficulties.

Subwavelength gratings have shown promising results when applied to a number of different waveguide couplers including directional couplers, adiabatic couplers, and multimode interference couplers. Directional couplers have traditionally suffered from limited bandwidth due to the wavelength-dependent nature of the beat length [30]. Subwavelength gratings were integrated into a directional coupler as shown in Figure 4 A with longitudinal gratings superimposed on the directional coupler in the coupling region. This idea was first explored in [31], where the superimposed subwavelength grating allowed for a fivefold enhancement of bandwidth in a 50/50 directional coupler. Subwavelength gratings were then used to increase bandwidth in directional couplers with different splitting ratios [32]. Adiabatic couplers tend to suffer mainly from the size of their footprint, as they must be long to ensure adiabadicity [6]. They operate via the interaction of modes in adjacent waveguides, so subwavelength gratings have been used to change the

effective index in the area between the two waveguides to decrease local confinement, increasing mode interaction, as shown in Figure 4 B. This allows the couplers to be made shorter [33], [34]. In multimode interference couplers, the use of subwavelength gratings has been shown to both increase bandwidth and decrease device footprint [35], [36].

Subwavelength gratings have been shown to enhance the sensitivity of multiple photonic sensor topologies. The two main mechanisms used in photonic sensing are bulk and surface sensing. In bulk sensing, the effective index of a waveguide segment or resonator changes due to a change in the index of the surrounding medium. In surface sensing, the surface is functionalized to adsorb specific molecules, and the effective index of the sensor changes as the thickness of the adsorbed layer increases [37]. In both cases, the sensitivity depends on the overlap between the evanescent tails of the propagating mode and the sensor's surroundings, so reducing the mode confinement of the sensor increases its sensitivity. This can be accomplished by reducing the effective refractive index of the sensor by making the sensing element out of a subwavelength grating [30]. In some implementations of this, the sensing elements were straight, cavity sensors as shown in Figure 4 C [38], [39]. Ring resonator sensors were also fabricated from subwavelength grating structures, shown in Figure 4 D [40], [41]. There is, however, a tradeoff between increased sensitivity and roughness-induced scattering in the subwavelength grating sensing elements [42].

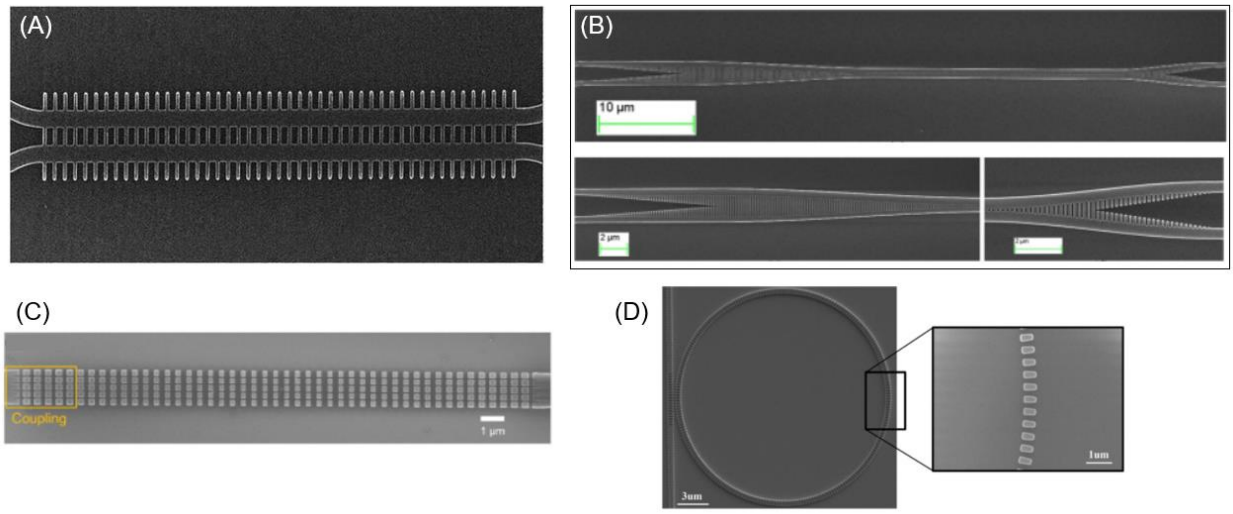

Figure 4. (A) SEM image of a directional coupler with superimposed subwavelength grating, allowing for a wider bandwidth [32] (B) SEM image of an adiabatic coupler with sections of subwavelength grating, enabling a smaller footprint [33] (C) SEM image of a photonic cavity sensor with subwavelength grating elements [39] (D) SEM image of a ring resonator photonic sensor made using subwavelength gratings [41]

Off-chip couplers (typically fiber-to-chip couplers) are an essential component to most photonic integrated circuits. Coupling between off-chip fibers and on-chip waveguides has historically been a challenge due to the size mismatch between the mode field diameters of waveguides and optical fibers [30]. The two main types of off-chip couplers are edge couplers and surface or grating couplers. Edge couplers are relatively simple, broadband couplers, but as their name implies, they can only be placed at the edge of a chip. The mode size mismatch between the fiber and waveguide is a particularly egregious source of loss. Subwavelength gratings have been used to decrease the effective refractive index of the waveguide near the edge, as shown in Figure 5 A. This increases the size of the mode propagating in the waveguide, decreasing the mode mismatch and allowing for a higher efficiency (upwards of 90%) [43], [44]. Grating couplers enable vertical off-chip coupling, as shown in Figure 5 B, and operate based on resonant coupling. Subwavelength grating structures have been used in grating couplers to improve efficiency by increasing mode overlap using their ability to adjust effective index, similar to edge

couplers with subwavelength grating elements [45]. The addition of subwavelength grating elements to grating couplers can also increase bandwidth and add polarization insensitivity among other applications [46], [47].

Flat optics are an application for subwavelength gratings that hasn't been fully explored, mainly due to the small feature sizes required for subwavelength gratings designed for NIR, visible and ultraviolet wavelengths. Spot size converters, which are essentially on-chip, waveguide-integrated lenses, have already been implemented with subwavelength gratings, as shown in Figures 5 C and D. The width of the grating elements is modulated to give the spot size converter a higher index towards the center, allowing for effective mode size change with a high bandwidth and low loss [28]. There have also been a handful of implementations of vertical, off-chip optics using subwavelength gratings. Ghargi *et al.* designed and fabricated an invisibility carpet cloak device implemented using subwavelength grating elements. This subwavelength grating consisted of a planar nitride waveguide with a pattern of subwavelength holes formed via electron beam lithography and reactive ion etching, as shown in Figures 5 E and F. The diameter and spacing of the holes determined local effective index, and the index pattern was designed using quasi conformal mapping to cloak a bump in the nitride film [48]. Later, Ye, Ray, and Yi designed, fabricated, and tested a flat, GRIN microlens made up of subwavelength gratings. The microlens had a bandwidth encompassing most of the visible spectrum (250 nm range) and was achromatic over this range. This particular microlens, shown in Figure 5 G, was fabricated from a low index E-beam photoresist polymer rather than silicon. The E-beam lithography process used was still direct write and low-throughput, but fabrication was less complex than for high contrast dielectrics such as TiO_2 or GaN [49].

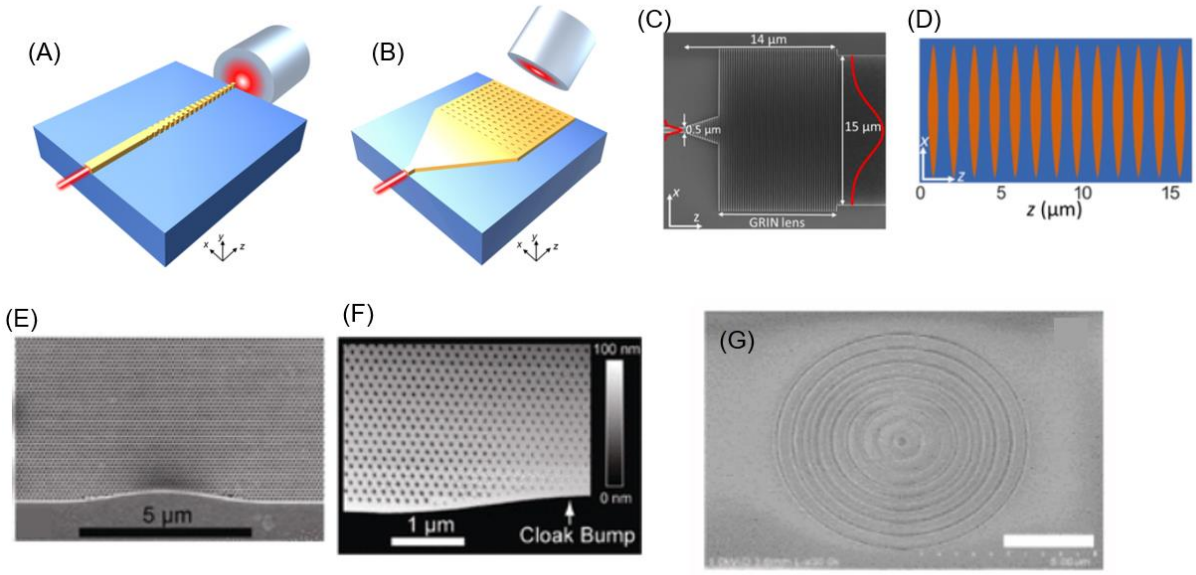

Figure 5. (A) edge coupler fabricated from a subwavelength grating [6] (B) grating coupler with subwavelength grating elements [6] (C) SEM image of a GRIN spot size converter fabricated from subwavelength gratings [28] (D) diagram of the GRIN spot size converter showing the shape of the subwavelength elements [28] (E) and (F) SEM images showing the surface of the invisibility carpet cloaking device fabricated [48] (G) SEM image showing the subwavelength grating flat microlens along with a 2.5 µm scale bar [49]

1.5 Subwavelength Grating Fabrication

As previously mentioned, the fabrication of subwavelength grating-based optics is difficult due to the small feature sizes required, particularly for devices designed for NIR, visible and UV wavelengths. As indicated in Figure 6, the main processes used for subwavelength grating fabrication are deep UV lithography, electron beam lithography, and extreme UV lithography [50]. Deep UV lithography is a mature, wafer-scale photolithography process that uses light in the UV-C band, which is between 100 and 280 nm. It is a mature technology capable of fabricating submicron features, but it is incapable of fabricating sub-100 nm features due to wavelength constraints. This range of feature sizes is suitable for creating subwavelength gratings designed for mid-infrared region [50]. Electron beam lithography is a direct write process that uses a focused, sub-micron-diameter beam of electrons to create patterns in a specialized resist [51]. It

has a higher resolution than deep UV lithography, but its low throughput limits its applications in subwavelength grating devices, especially if they are to be mass-produced. Extreme UV lithography is a largely experimental process that has the potential to pattern wafer scale patterns with sub-100 nm features. It is similar to deep UV lithography but with a shorter wavelength, which leads to some added challenges that have delayed its commercialization. Due to the extremely short wavelengths of EUV sources (13.5 nm or less), EUV photons are easily absorbed by almost any medium. This leads to challenges in choosing materials for EUV masks and resists and also means that the EUV chamber must be kept at a high vacuum. Additionally, EUV sources must have very high power, a challenge that has mostly been solved through the use of laser and discharge produced plasmas [52].

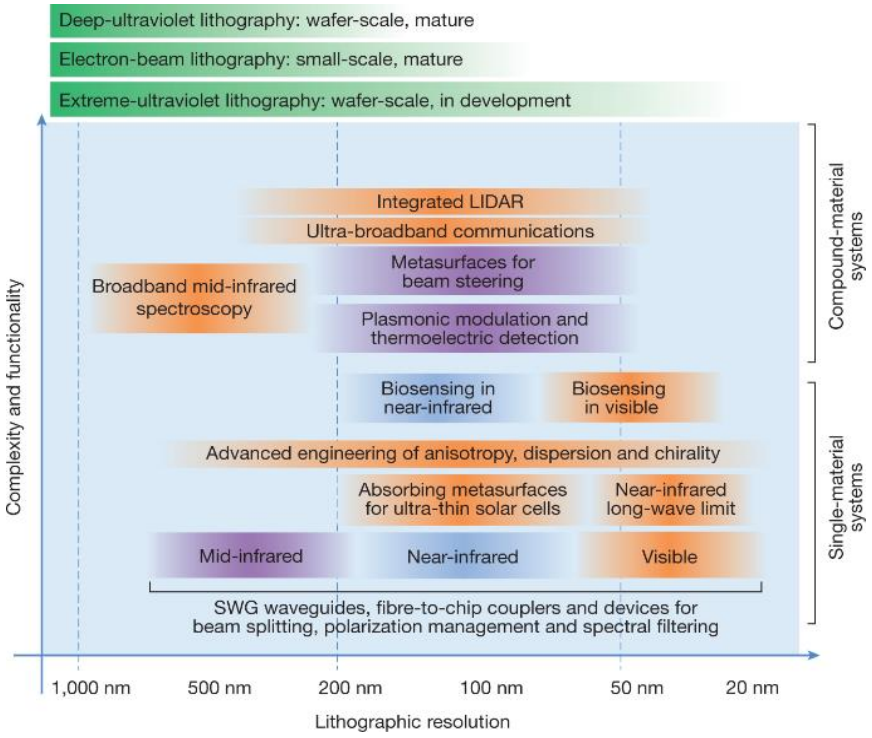

Figure 6. Diagram of subwavelength grating applications and fabrication techniques [50]

CHAPTER 2

THE NANOIMPRINTING OF REFRACTIVE INDEX PROCESS

Although subwavelength gratings are a promising technology for a variety of applications, the fabrication difficulties detailed in the previous chapter prevent them from widespread use. An alternative to the top-down manufacturing of subwavelength gratings involves leveraging bottom-up, self-organization techniques that are present at subwavelength scales. The subwavelength-scale of the self-organized structures gives them an effective refractive index similar to subwavelength gratings. Some recent examples of bottom-up techniques used to create effective refractive index profiles are ionic exchange in chalcohalide glass composites ($\Delta n < 0.1$) [53], UV exposure on photosensitive glass based composites ($\Delta n < 0.01$) [54], micro-contact photothermal annealing of organic/inorganic hybrid materials ($\Delta n \approx 0.05$) [55], direct electrospray printing of chalcogenide glass films ($\Delta n < 0.4$) [56], densification of Si or TiO2 based nanocomposites in UV curable films ($\Delta n < 0.45$) [57], and electrochemical etching of mesoporous silicon [58] ($\Delta n < 2$). Of these techniques, those involving anodized mesoporous silicon, which features deeply subwavelength pore diameters in the range from ~2 – 50 nm is especially attractive due to its high index contrast and CMOS compatible synthesis from silicon wafers [59].

The nanoimprinting of refractive index (NIRI) process is a nanoimprint lithography technique specifically applied to mesoporous silicon [60]. As will be demonstrated in subsequent chapters, this process is capable of producing flat porous silicon films with arbitrary effective refractive index profiles with a high degree of control. The NIRI process is promising for the field of flat optics in particular because it offers the effective index patterning flexibility of subwavelength gratings while also being high-throughput and inexpensive by utilizing the bottom-up self-organization of mesoporous silicon. There are a variety of other processes for fabricating

porous silicon structures, but none offer the large index range, GRIN patterning capability, and high throughput of the NIRI process. A generic outline of the NIRI process will be described in this chapter, while the specifics of fabricating microlenses and waveguides using the NIRI process will be discussed in chapters 3 and 4 respectively.

2.1 Properties of Porous Silicon

Porous Silicon was first reported in 1956 by Uhlir after he inadvertently fabricated it while electropolishing silicon wafers. There was an explosion of interest in it in the 1990's following Leigh Canham's publications on red luminescence of porous silicon [61]. Research interest in porous silicon persists due to its unique optical, electrical, chemical, and structural properties as well as its ease of fabrication. Major avenues of porous silicon research include electronics, optoelectronics, optics, diagnostics, medical applications, and energy applications [62].

Although there are a number of methods for fabrication of porous silicon, the concentration of this thesis will be on the formation of mesoporous silicon by the anodization of p^+ (1 0 0) silicon wafers. In this process, the silicon wafer itself serves as the cathode, and platinum wire is used for the anode. A fluoride-based electrolyte, usually hydrofluoric acid, is required to etch pores into the surface of the silicon [63]. When a uniform current density is applied to the cell, an oxidation reaction occurs on the silicon surface, resulting in pore formation. The curve in Figure 7 A models the Si/HF system, showing how the general current density of the system changes in response to applied potential. The point denoted 'OCP' is the open circuit potential of the silicon electrode. Above the open circuit potential point, the silicon electrode enters the region corresponding to the formation of porous silicon. After a transition region where both pore formation and electropolishing mechanisms are present, the silicon enters a purely electropolishing region, where the surface is eroded uniformly without pore formation.

The primary oxidation reaction in the porous silicon region is the following half-reaction:

$$\mathrm{Si} + 6\mathrm{F}^- + 2\mathrm{H}^+ + 2\mathrm{h}^+ \rightarrow \mathrm{SiF}_6^{2-} + \mathrm{H}_2 \quad (15)$$

Here, h^+ represents a valence hole in the silicon while H^+ represents a proton [64]. In addition to the formation of pores on the silicon surface, this reaction leads to the formation of hydrogen gas bubbles, which can limit the etching reaction if they become stuck to the porous silicon surface. In order to prevent this, surfactants are often added to HF electrolyte solutions. Typically, these surfactants are a type of alcohol such as ethanol or methanol [63]. The dissolution rate of silicon according to this reaction depends on the exposed crystal plane. The (100) crystallographic plane is especially prone to pore formation reactions due to the strained S-H bonds in this plane, making (100) silicon wafers ideal for the formation of porous silicon films. Once a pore forms in the (100) surface, it propagates perpendicularly because the enhanced electric field at the pore tip attracts holes, which fuel the reaction in equation 15. The porous silicon layer isn't completely etched away during the etching process because of the crystallographic orientation of the pore sidewalls as well as the dearth of holes near the surface of the pore sidewalls, which limits the etching reaction [64].

A number of anodization parameters can be used to control the formation of (100) porous silicon films. For instance, when an alcohol surfactant is used to dilute the HF electrolyte, the porosity of the anodized film can be controlled by the concentration of HF relative to surfactant [63]. The porosity can also be controlled by modifying the applied cell current. For a larger applied cell current, the porosity and average pore size of the film increases. Additionally, the pore size distribution of the film also increases with increased current density [65]. The depth of the porous silicon film can be controlled by the amount of time that the current is applied or by the current density, with higher current densities causing higher etch speeds [59]. Due to the

importance of holes in the etching process, the doping density of the p-type silicon also effects the pore formation. Highly doped p-type wafers form pores with larger diameters, while silicon wafers with lower p-type doping form smaller pores [65].

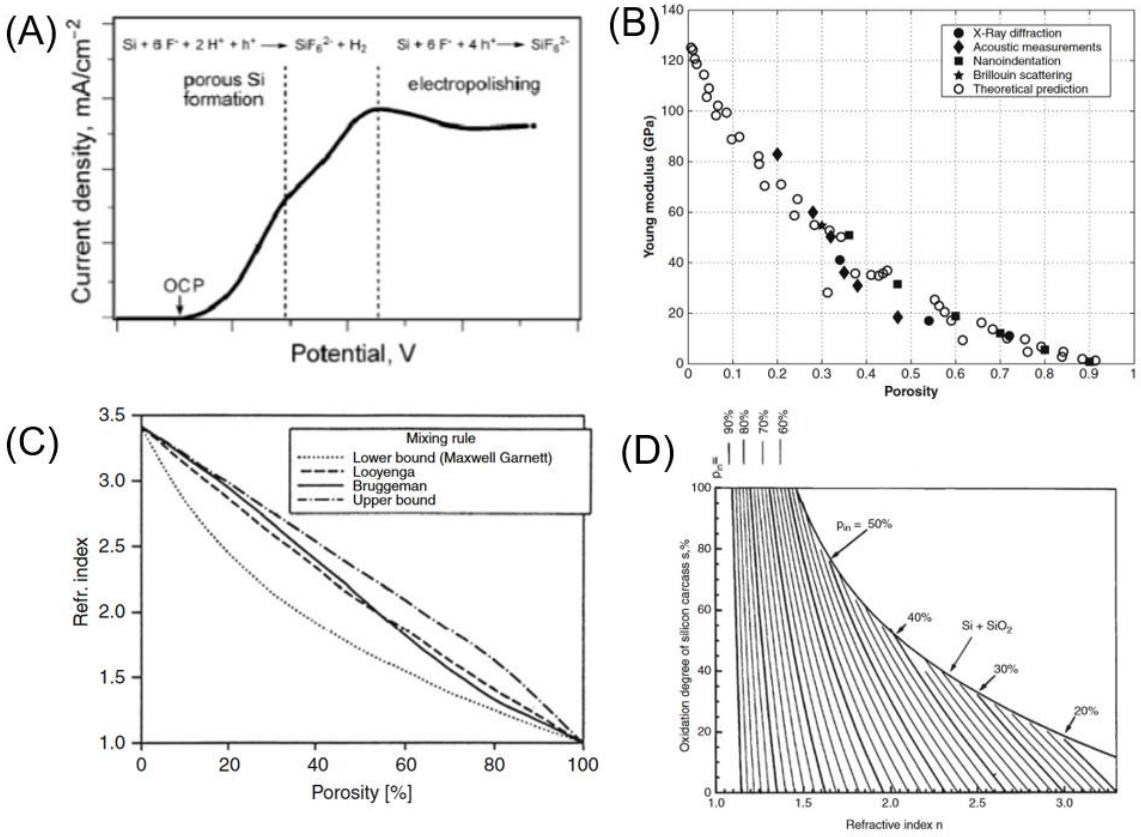

Figure 7. (A) approximate trend showing applied etching cell potential vs. current density in the Si/HF system. The region on the left is where porous silicon forms. After the first threshold, the surface is more uniformly etched away [64] (B) Variation of Young's Modulus with porous silicon film porosity according to several different measurement methods [66] (C) Graph showing how the theoretical predictions of the Bruggeman approximation, Looyenga equation, and Maxwell-Garnett mixing rule vary with film porosity [58] (D) calculated curve showing the variation of refractive index with silicon dioxide skeleton fraction in a porous silicon film, measured at 632.8 nm wavelength; calculations were performed using a 3-component Bruggeman approximation [67]

Porous silicon, similar to other porous materials, possesses a number of unique properties, many of which are tunable based on the porosity and/or pore diameter of the porous silicon film. In terms of structural and mechanical properties, the porosity of the film determines its surface area, density, hardness, Young's modulus, and fracture toughness [68]. In a p^+-doped mesoporous

film, as the porosity varies from 30% to 84%, the Vickers hardness value varies between 8.8 GPa and 0.75 GPa, a reduction of more than 90% [69]. As the porosity of a p^+-doped mesoporous silicon film increases, the Young's modulus of the film varies according to the trend shown in Figure 7 B [66]. Due to the anisotropic structure of anodized, mesoporous p^+ (100) silicon films, they display anisotropic mechanical behavior. For instance, mesoporous silicon films have been shown to have different values of Young's modulus when tested in different directions relative to the pore direction [70].

Porous silicon's unique optical properties have been of particular interest over the previous few decades. At visible wavelengths and above, mesoporous silicon can be described by an effective permittivity tensor, similar to equation 4, due to its subwavelength-diameter pores, which vary from 2 to 50 nm, as well as its structural anisotropy. For (100) mesoporous silicon, the refractive index experienced by light perpendicular to the film surface is different from that experienced by light shining perpendicular to the pore walls [71]. The effective index models used for subwavelength gratings cannot be used for mesoporous silicon due to the irregularity of the pore structure. There are some more appropriate models such as the Bruggeman approximation, the Looyenga formula, and the Maxwell-Garnett mixing rule [58]. The Bruggeman approximation has been found to fit experimental data from etched, meso-porous silicon samples [72]. The goodness of fit of a given model depends on the porous silicon film structure as well as its porosity, as shown in Figure 7 C [58]. As can be seen from the graph, the refractive index of the porous silicon film varies between that of bulk silicon and that of air. For porosities between 30% and 80%, the refractive index of a silicon-supported, mesoporous (100) silicon film ranges between ~2.8 and ~1.4, an index contrast > 1 [73]. Porous silicon naturally forms a native oxide in an oxygen-heavy environment, which decreases the refractive index as shown in Figure 7 D.

Porous silicon also possesses unique electrical and chemical properties. One notable property of porous silicon is its resistivity, which is 5 orders of magnitude greater than that of bulk silicon. This is due to the depletion of holes from the surface of the silicon skeleton during the etching process. The conductivity of a porous silicon film can be tailored by changing its porosity, though the conductivity is also strongly dependent on the properties of the bulk silicon prior to anodization [74]. Porous silicon is also both biocompatible and biodegradable, which has excited interest for its use in biosensing [75]. Furthermore, the surface of porous silicon tends to have a large number of Si-O bonds due to native oxide formation as well as some Si-N and Si-C species. All three of these bonds are very stable and can be used to attach a number of functional molecules to the surface for sensing applications [76].

Porous silicon has been the subject of research for a variety of applications. Currently, the most actively researched include sensing, energy conversion, micro-optics, and various biomedical applications [62]. Most porous silicon sensors are photonic sensors such as those discussed in the previous chapter, where changes in resonance of the porous silicon photonic element indicate changes in either adsorbed molecule layer thickness or the index of the surrounding medium [77]. The capability and cost of these sensors are highly dependent on the fabrication techniques used to create the photonic sensing elements from the porous silicon film. Porous silicon is also being researched for use in battery electrodes, solar cell anti-reflective coatings, and fuel cells. In biomedical applications, porous silicon is being researched for use in drug delivery, orthopedics, and tissue engineering [62]. In the realm of micro-optics, porous silicon has been fabricated into a range of different devices including photonic crystals, optical waveguides, and diffraction gratings. These also require porous silicon microfabrication techniques, many of which are low-throughput and insufficient for large-scale production.

2.2 Porous Silicon Fabrication Techniques

Despite the potential of porous silicon as a material, it is difficult to manipulate and pattern using traditional microfabrication techniques. It is difficult to pattern porous silicon using photolithography because resists, developers, and etchants become stuck in pores, causing issues in both positive and negative photolithography [78], [79]. Both wet and dry etching of porous silicon are also rendered impractical by the pore morphology [78].

Traditional photolithography techniques are sometimes still used along with backfilling and capping layers, but there are also microfabrication techniques developed specifically for porous silicon that avoid the poor fidelity, over-etching, and poor sidewall control of porous silicon photolithography [78], [79]. Most of these focus on pre-processing of the silicon substrate prior to the formation of the porous layer. For instance, ion irradiation can be used to locally modify silicon doping, which modifies subsequent pSi porosity. It allows for some degree of depth control, but it is generally a very low throughput process [80]. Dry Removal Soft lithography (DWSL) utilizes a soft PMDS stamp to selectively lift off parts of the porous silicon film, but is restricted to binary, 2D patterning of the film [81]. Mac-Imprinting uses metal-assisted chemical etching to selectively etch parts of the porous silicon surface [78]. This changes the height of the film in a continuous manor but doesn't actually compress it or change the local refractive index.

This can be useful in some applications, however when local changes in refractive index are necessary, there are some appropriate microfabrication methods. These methods are the direct imprinting of porous substrates (DIPS) and nano-imprinting of refractive index (NIRI) processes, both of which involve mechanically compressing select areas of a porous film to change the local height and porosity [60], [82]. Unlike the DIPS process, the NIRI process has almost exclusively been applied to porous silicon with the primary aim of changing the local refractive index of the

porous silicon film by compressing the silicon skeleton [60]. The DIPS process has shown the feasibility of creating curvilinear structures, shown in Figure 8 A and B, and both processes have been used to demonstrate optical grating structures, shown in Figure 8 D and E [83]. These processes are very high throughput and can be performed at room temperature without the need for pre-processing of the porous substrate for patterning. Additionally, the refractive index patterning these processes provide is extremely flexible, and can be made into gradient, pixelated, or binary patterns as desired [60], [82].

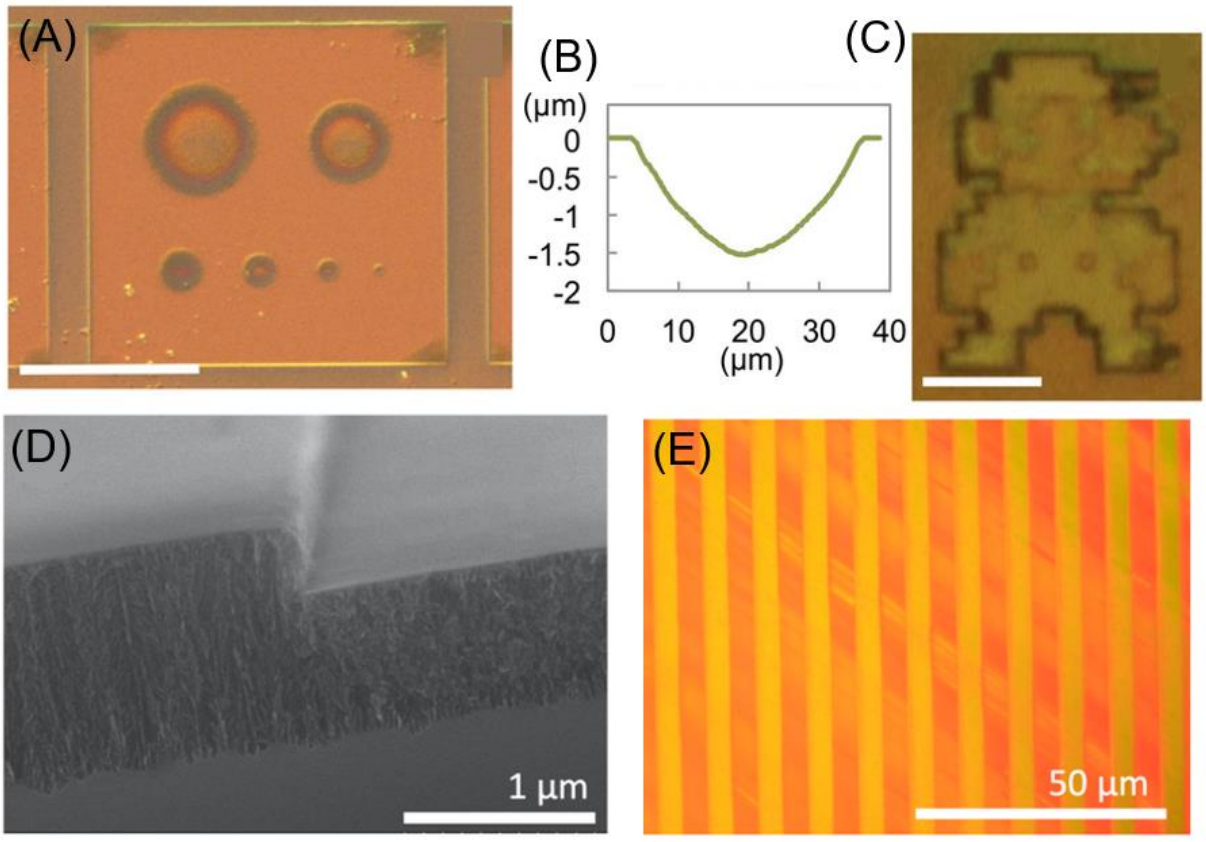

Figure 8. (A) Optical microscope image of a curvilinear structure created in porous silicon using the DIPS process; the scale bar is 100 μm [84] (B) AFM line scan of one of the curvilinear structures pictured in (A) [84] (C) optical microscope image of a multilevel, digital pattern created using the DIPS process; the scale bar is 10 μm [84] (D) SEM image cross-section of a grating structure created using the NIRI process, showing the densification of the porous silicon structure [60] (E) Optical microscope image of a grating structure created using the NIRI process and then planarized; the structural color of the film indicates the pattern of refractive index [60]

A useful potential application of this fabrication technique is the manufacture of flat optics. As previously mentioned, most flat optics are currently implemented using diffractive optics, metasurfaces, or subwavelength gratings. These approaches face significant manufacturing difficulties, particularly metasurfaces and subwavelength gratings, which require deeply subwavelength lithography techniques. In addition to low throughput and high costs, these lithography techniques also have the downside of being binary patterning processes, so analog patterning over a device surface is difficult to accomplish. NIRI flat optics could provide a continuous variation in refractive index combined with a high throughput.

Porous silicon is not a completely novel material in the manufacture of flat optical lenses, but previous approaches have demonstrated some significant downsides. For instance, many of these require etching or selectively doping of the silicon substrate in a particular pattern prior to anodization in order to create a graded refractive index [85]–[87]. These planar microlens fabrication methods require more processing steps, inherently lowering throughput, and also don't report particularly high index contrast for lenses fabricated. Ilyas and Gal reported fabrication of planar, pSi GRIN lenses using a specialized ring-shaped electrode during anodization [88], [89]. Due to the electrical properties of silicon, the circular lens profile was limited to a quadratic profile unless additional masking steps were used. The NIRI process overcomes the downsides of previous pSi GRIN microlens implementations, as it allows for rapid and easy fabrication with a large index contrast exceeding $\Delta n = 1$ and an arbitrary index pattern [60].

2.3 Details of the Nanoimprinting of Refractive Index Process

Figure 10 A depicts an overview of the NIRI process, wherein a premastered and reusable stamp is utilized to compress a mesoporous silicon film, patterning the refractive index distribution $n(x,y)$. This study used the previously-characterized NIRI procedure to fabricate two different

types of devices from mesoporous silicon (pSi) films [60]. The NIRI process allows for localized changes in refractive index through the compression of the silicon skeleton of the mesoporous film, effectively decreasing its porosity. The refractive index profile of the resulting compressed film is dependent on the geometry of the stamp used and can produce both binary and gradient refractive index profiles. The two NIRI devices fabricated in this study, optical waveguides and flat, gradient index microlenses, utilized binary and grayscale stamps respectively. As previously discussed, prior work exploring the NIRI process has demonstrated a microscale binary grating pattern as a proof of concept, pictured in Figure 8 E and F, but did not demonstrate greyscale refractive index patterning or the operation of an optical device fabricated using NIRI [60].

Previous work has characterized the NIRI refractive index change as it varies with compression and demonstrated that a refractive index change of $\Delta n \approx 1$ is possible through the NIRI imprinting process [60]. The initial porosity of the pSi determines the maximum imprint fraction as well as the resulting refractive index at a given pressure. The initial porosity also determines the range of achievable refractive index changes, so a larger starting porosity allows for a greater refractive index change from imprinting due to a larger void fraction. The pSi samples used in device fabrication for this experiment were p-type (1 0 0) wafers with a conductivity between 0.01 and 0.02 Ω-cm, etched in a 15% ethanoic HF solution using a current density of 55.1 mA/cm^2. This resulted in films with an approximate thickness of 1.1 μm and an approximate starting porosity of 75%. The average pore size for these samples, since they were mesoporous (1 0 0) silicon, was between 2 and 50 nm, which is significantly smaller than the test wavelengths of 406 to 635 nm for the microlenses and 1260 to 1360 nm for the waveguides. Due to the subwavelength nature of the pores, an effective medium approximation for porous silicon films was used to describe the mesoporous film for simulation purposes. The main approximations used

for porous silicon were discussed in the first section of this chapter. In previous work on the NIRI process, it was found that a modified, 3-component Bruggeman effective medium approximation provided the best fit for the raw data extracted from NIRI-imprinted porous silicon films [60]. This approximation accounts for the silicon skeleton, air, and native SiO2 layer. The standard, 2-component Bruggeman approximation is as follows:

$$(1-p)\frac{n_{\mathrm{Si}}^2-n^2}{n_{\mathrm{Si}}^2+2n^2}+p\frac{1-n^2}{1+2n^2}=0$$

(16)

Where n is the effective refractive index of the porous silicon film, n_{Si} is the refractive index of silicon, and p is the volume fraction of the pores [67]. This formula is applicable to freshly anodized porous silicon films with relatively high porosities but is insufficient for describing porous silicon films that have undergone oxidation in ambient conditions. The oxidation of the film leads to significant volume expansion of the skeleton in addition to a decrease in the silicon volume fraction. Assuming the non-oxidized silicon volume fraction in a porous silicon film is $f_0 = 1\text{-}p_0$, where p_0 is the initial pore volume fraction, a fraction x of f_0 is oxidized under ambient conditions. The formation of silicon dioxide causes an expansion by a factor of ~2.27, so the volume fraction of SiO_2 is $g = 2.27x$, the new volume fraction of silicon is $f = f_0 - x$, and the new pore volume fraction is $p = 1 - f - g$ [67]. The unmodified, 3-component Bruggeman equation is as follows:

$$(f_0-x)\frac{n_{\mathrm{Si}}^2-n^2}{n_{\mathrm{Si}}^2+2n^2}+2.27x\frac{n_{\mathrm{SiO2}}^2-n^2}{n_{\mathrm{SiO2}}^2+2n^2}+(1-f_0-1.27x)\frac{1-n^2}{1+2n^2}=0$$

(17)

Figure 7 D shows how the index n varies with increasing SiO_2 volume fraction according to this model.

The Bruggeman approximation detailed above does not explicitly account for film compression. The derivation of the effective medium formula applied to the NIRI process is as follows. In the NIRI process, the imprinted porous silicon film has a desired refractive index profile: $n(x,y) = n_0 + \Delta n(x,y)$. The index of the compressed film is dependent on the compressed height of the film: $h(x,y) = h_0 + \Delta h(x,y)$, where h_0 is the initial film thickness and Δh describes the imprint depth, which is dictated by the geometry of the stamp used. In NIRI, the local porosity P is decreased by inducing a net volume reduction ΔV of a defined porous medium volume V_0, according to:

$$P = 1 - \frac{1 - P_0}{1 - C}$$

(18)

Where C describes the volumetric expansion of the underlying film according to:

$$C = -\frac{\Delta V}{V_0} \approx -\frac{\Delta h}{h_0}$$

(19)

Here, the quantity $\frac{\Delta h}{h_0}$ is the engineering strain of the compressed film. The above approximation can be made because the transverse strain, $\frac{\Delta w}{w_0}$, representing the width expansion of the compressed film, and therefore the Poisson ratio $v = \frac{\Delta h}{\Delta w}$, is negligible for larger imprinted features, as demonstrated in Figure 9 C through E. Although smaller digital features such as the 0.35 μm wide waveguide in Figure 9 B were fabricated, the simulation and testing in this project focused on 2-μm or wider digital and gradient imprints.

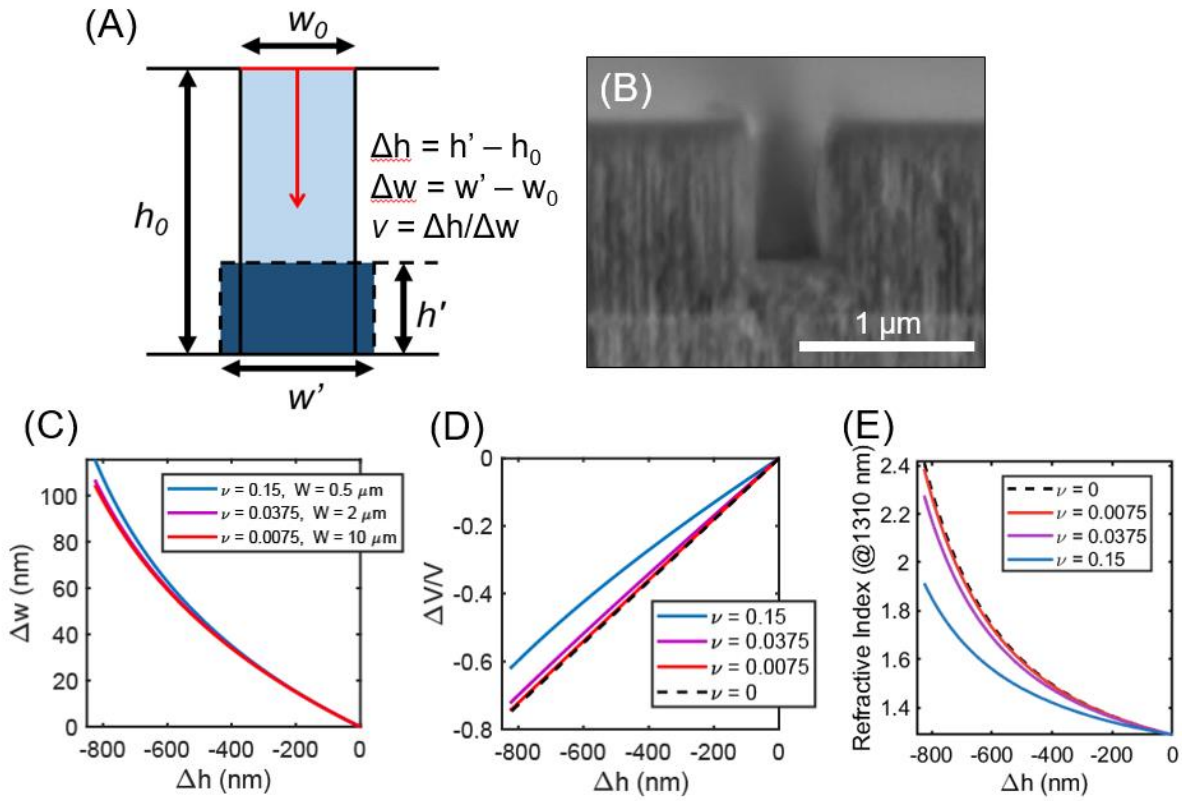

Figure 9. (A) A diagram showing the Poisson effect for an isolated digital imprint, (B) SEM image of a ~350 nm wide digital imprint exhibiting a small amount of lateral expansion in the high compression (deformation) regime, indicating a low Poisson ratio. (C) Calculated lateral expansion of 500 nm, 2000nm, and 10,000 nm wide digital features under Poisson ratios of 0.15, 0.0375, 0.0075. To achieve the same ~100 nm lateral expansion near high compression, the Poisson ratio is effectively feature size dependent. (D) Calculated normalized volume change for digital imprints with different Poisson ratios. (E) Expected refractive index for digital imprints with differing Poisson ratios (v). Deviation from 0 Poisson ratio (ZPR) coincides with non-negligible lateral expansion and reduction in refractive index relative to the ideal ZPR value.

The post-imprint porosity distribution of the NIRI-imprinted film is $P(x,y)$, which is related to the imprint profile $h(x,y)$ according to the following formula:

$$P(x,y) = 1 - \frac{h_0}{h(x,y)}(1 - P_0) \quad (20)$$

Where the post-imprint height and porosity are bounded by: $h_0(1 - P_0) \leq h \leq h_0$ and $0 \leq P \leq P_0$ respectively. To simplify the 3 component Bruggeman approximation as a function of porosity,

the quantities of n_{Si} and n_{SiO2} from equation 17 were lumped into a single value, n_{sk} representing the effective refractive index of the skeleton. It was assumed that the silicon skeleton was comprised of a 50:50 volumetric ratio of SiO_2 to Si. The simplified Bruggeman approximation as a function of porosity is as follows:

$$P(x,y)\frac{1-n_{sk}^2}{1+2n_{sk}^2}+\big(1-P(x,y)\big)\frac{n_{sk}^2-\big(n(x,y)\big)^2}{n_{sk}^2+2\big(n(x,y)\big)^2}=0 \qquad (21)$$

Figure 10 C shows how the effective refractive index of a NIRI imprinted film changes with imprint fraction and porosity according to this model. As indicated in the figure, the refractive index can be controlled over a wide working range Δn, readily reaching from ~0.5-1 RIU at optical wavelengths (e.g. λ_0=635 nm). The maximum achievable film refractive index is determined by the refractive index of the skeleton, while the achievable index contrast is determined by the initial porosity P_0.

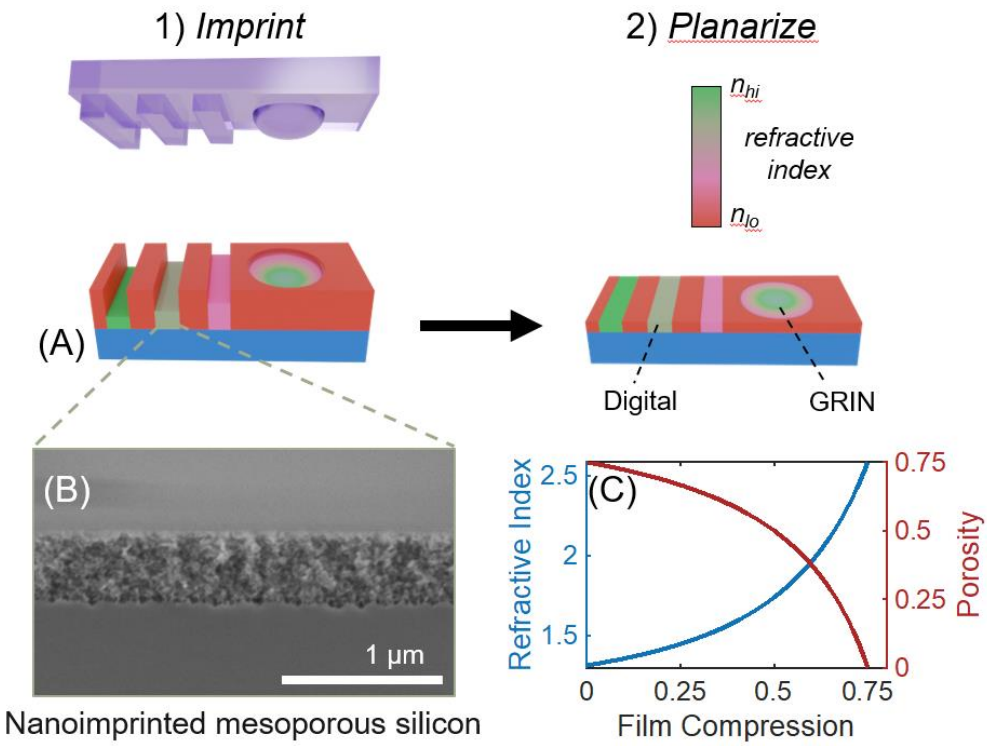

Figure 10. (A) This diagram shows a simplified procedure for NIRI device fabrication (not to scale). A solid silicon or fused silica stamp is pressed into the porous silicon following HF etching, and then the porous silicon is polished to achieve flat optical or photonic devices. The areas in pink and green indicate a higher refractive index achieved through imprinting (B) SEM image of a post-imprinted pSi film (C) Evolution of porosity *P* and effective refractive index *n* vs. film compression *C* assuming $P_0 = 0.75$ and a skeleton comprised of 50:50 $Si:SiO_2$

As an additional case study in the index patterning ability of the NIRI process, an extra pSi sample was prepared following the standard NIRI procedure used in this paper. It was then imprinted with a solid piece of silicon wafer at a pressure of 642.97 N/mm^2, significantly reducing the porosity in the imprinted area. The imprinted areas on the actual NIRI fabricated devices were too small to gather useful reflectance data given the available equipment. Figure 10 B shows an SEM cross-section of the porous silicon after it was imprinted from an initial height of 1.143 μm to a final height of 0.433 μm, an imprint fraction of $C = 0.61$. The refractive index of the film before and after imprint was determined using reflectance measurements, pictured in Figure 11. The reflectance traces were fit using the standard 3-component Bruggeman NIRI model, which

indicated an index contrast of $\Delta n = 0.85$. Furthermore, both reflectance traces in Figure 11 also show minimal attenuation over the 500 nm wavelength range, indicating that losses and scattering are not particularly strong factors. This confirms that the mesoporous silicon film acts as an effective medium for wavelengths over 500 nm regardless of imprinting.

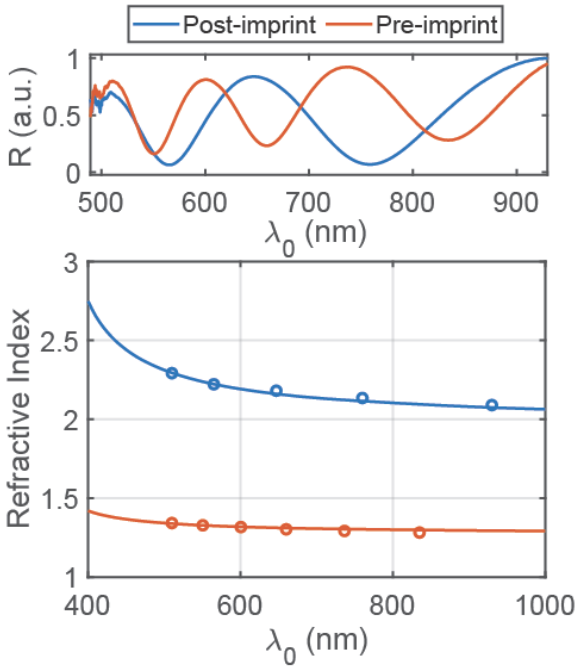

Figure 11. Reflectance data from imprinted and non-imprinted porous silicon film (top) as well as the fit refractive index of the pre- and post-imprint films over the 400 to 1000 nm range

CHAPTER 3

NANOIMPRINTED REFRACTIVE INDEX MICROLENS ARRAY

3.1 NIRI Microlens Fabrication

The specifics of the nanoimprinted refractive index (NIRI) microlens fabrication process are shown in Figure 13 below. The etch cell used in all of the etching stages is pictured in Figure 12. A 15% ethanoic hydrofluoric acid solution was used in all trials. The etch cell includes a platinum wire cathode, and the silicon wafer serves as the anode. The electrodes are connected to a Keithley 2601A SYSTEM SourceMeter current source controlled using Keithley etch system control software. The DC current density used in the initial etch phase for the microlens fabrication is 55.1 mA/cm^2, which is applied for 34 seconds, resulting in a ~1.1 μm porous silicon layer with an initial porosity ~0.75. The film is then imprinted with the microlens stamp, an off the shelf 5 mm x 5 mm fused silica microlens array (SUSS MicroOptics) comprised of a rectangular array of spherical cap features with a radius of curvature equal to 708 μm and a pitch of 110 μm. An approximate rendering of this stamp can be seen in Figure 14 A, though it is not to scale. This particular stamp showed remarkable durability, as we used it to create well over 50 microlens imprints at a pressure of ~4 kN before it began to crack. This indicates that fused silica is a promising candidate for use in stamps for larger-scale NIRI imprinting.

The imprint occurred at a pressure of ~4 kN for <5 seconds using a Specac Atlas 2T manual hydraulic press. To prevent cracking of the porous silicon sample during imprinting, both sample and stamp are backed with Scotch tape prior to imprinting. The porous silicon is placed in the hydraulic press with the porous layer facing up, and the stamp is placed on top of the porous layer face down. Figure 14 B shows an optical microscope image of the analog profile formed in the nanoimprinted mesoporous silicon film after imprinting with a force of ~4 kN for <5 sec. Further

details of the imprint methods can be found in Appendix A. The gradient pattern resulting from the imprint can be directly observed from the concentrically uniform and radially modulated structural color profiles captured by the microscope camera. Following imprinting, the microlenses are briefly annealed at 500°C for 15 minutes in air in order to prevent excessive scratching and deformation of the film during polishing. During this annealing phase, a thin oxide layer is grown on the internal surface of the silicon skeleton which passivates the film, increasing its hardness and durability, but there is still a significant amount of silicon present in the porous skeleton, an estimated fraction of 50%.

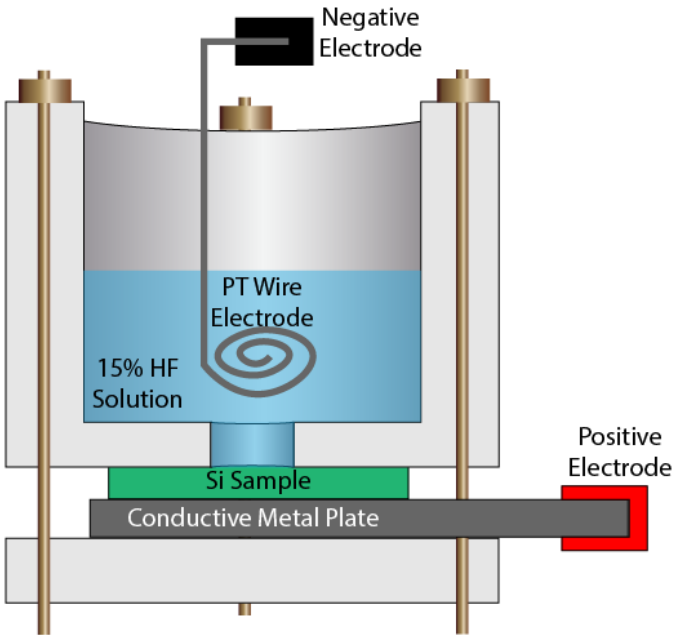

Figure 12. Schematic of the porous silicon etch cell used in the fabrication of NIRI devices (not to scale)

To realize a truly flat-optical structure capable of reshaping an incident wavefront according to its modulated refractive index profile $\Delta\phi(x,y) \propto \Delta n(x,y)$, we remove the imprinted surface topography of the microlens array by performing chemical mechanical polishing (CMP). We performed the polishing for these NIRI microlens samples using a Buehler VibroMet 2 vibratory polisher with a 0.06 μm colloidal silica slurry (pH = 9.8). An issue with this particular polishing

process was the insufficient planetary motion of the sample during polishing, which gave rise to uneven polishing and polishing gradients across the sample in some cases. We partially compensated for this by manually rotating the samples in the polisher relative to the direction of revolution periodically throughout the polishing process. Further details on the polishing methods can be found in Appendix B. A 50-minute polish using this method was found sufficient to planarize the film to a final thickness of ~320 nm. Due to the thinness of the film, we etch a thicker, mechanical support porous layer beneath the porous GRIN layer following polishing. This mechanical support layer is created using a slightly lower current density of 52 mA/cm^2 because the higher current density was found to cause structural collapse in the porous silicon film. We perform a third etch to separate the planar microlens array from the solid silicon substrate. The current density used in this etch stage is 137.8 mA/cm^2, more than twice the current density of previous stages. This causes the etching to proceed in the electropolishing regime, shown in Figure 7, so a thin layer of silicon is removed uniformly at the support layer-substrate interface. Due to the short duration of this etch phase, the high etch current density doesn't significantly degrade the porous silicon layers. We then lift off the microlens film onto optically transparent, double-sided adhesive (Nicomatic transparent spacer adhesive), adhered to a borosilicate glass coverslide (22x22 #1 Platinum Line Cover Glass).

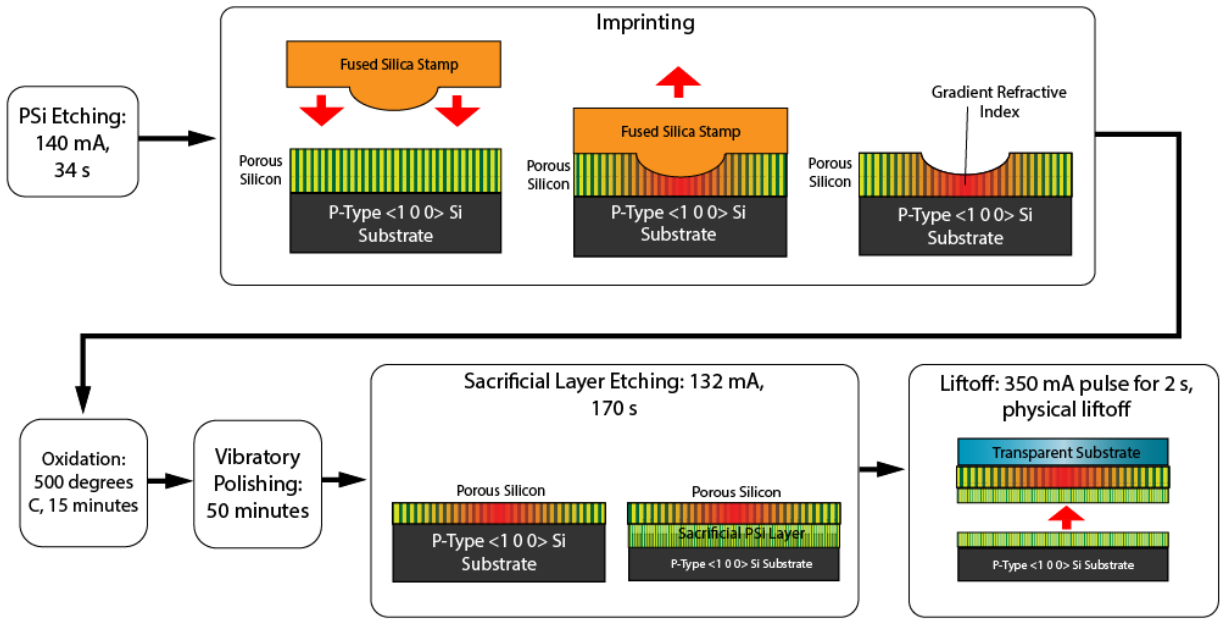

Figure 13. A flow chart depicting the process used to create a NIRI microlens array. Following NIRI imprinting, the lenses are briefly oxidized to prevent scratches in the vibratory polisher, after which they are planarized through polishing. A second round of etching is performed to form a mechanical support layer, which is fractured using a pulse in the electrochemical cell. After this, the microlens layer can be lifted off onto a transparent substrate, which was a microscope coverslide in this case; the red areas on the porous silicon layers indicate an area of densified film caused by the imprint process

Figures 14 C and d show the nanoimprinted mesoporous film at different points in the process shown in Figure 13. Given the flat nature of the planarized film, the structural color pattern observed in Figure 14 C and D arises purely from the patterned refractive index variation $\Delta n(x,y)$ modulating the local reflectance characteristics which are dictated by thin-film Fabry-Perot interference. As can be seen in Figure 14 C, there is some deviation from the perfectly circular lens profiles seen in the imprint image due to flaws in the vibratory polishing process that caused pore deformation and uneven polishing. Further improvements in polishing, such as more uniform planetary rotation of the sample during polish, will likely result in more perfectly circular planarized lenses. It should also be noted that the observed color profile of these GRIN patterns

spans a full 360-degree orbit through chromaticity space, which suggests NIRI could also be utilized to nanoimprint structural colors over a wide color gamut.

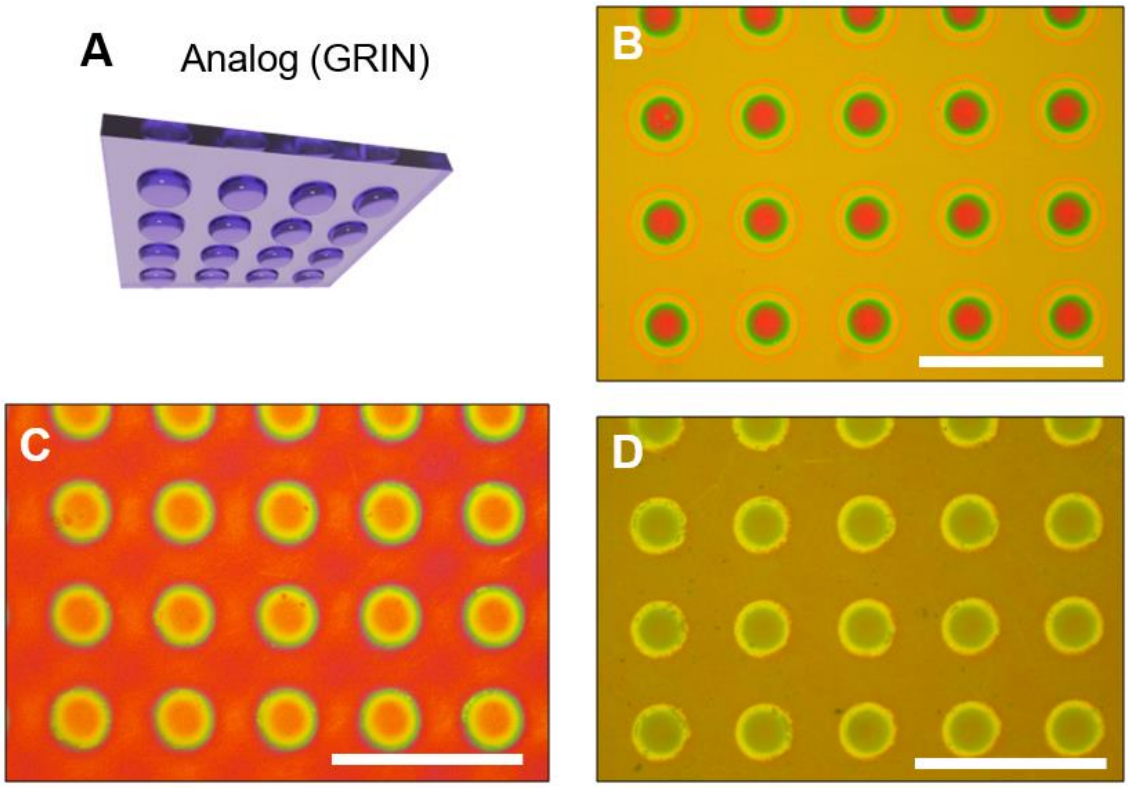

Figure 14. (A) An artistic rendering of an analog stamp profile in a fused silica microlens array stamp, (B) an optical microscope image of the microlens array imprint in a ~1.1 μm thick, ~75% porosity film (scale bar 200 μm), (C) a flat GRIN microlens array following 50 min CMP to a flat-optic thickness of ~320 nm prior to detachment from the substrate (scale bar 200 μm), (d) a flat GRIN microlens array following the mechanical support layer (~5μm thick) etch, just prior to detachment from the substrate (scale bar 200 μm).

To quantitatively measure the imprinted $n(x,y)$ profile prior to planarization, we performed multi-wavelength interferometry at wavelengths 406 nm, 520nm, and 635 nm in a customized reflection mode microscope setup. We then fit the experimentally observed fringe profiles (Figure 15 A through C) to a model (Figure 15 D through F) accounting for the patterned height $h(x,y)$ and dispersive gradient refractive index $n(x,y,\lambda)$ profiles. Our model fit shows excellent correspondence with the observed profiles as shown in Figure 15 G through I, and indicates that

the porosity of the patterned effective medium depicted in Figure 14 B is modulated from ~0.75 at the outer edge of the GRIN profile to ~0.315 at the center as shown in Figure 15 J and L. At the green test wavelength this corresponds to an analog GRIN profile $n(x,y)$ patterned with a dynamic range from ~1.35 to ~2.15 over a radial distance of ~35 μm.

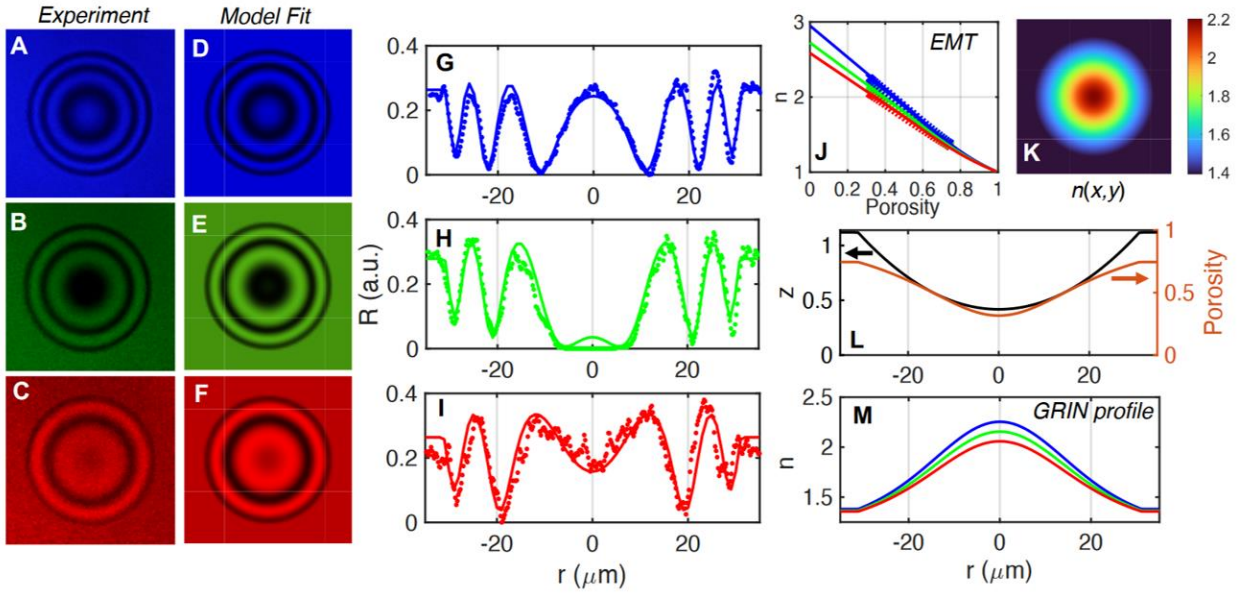

Figure 15. (A), (B), and (C) show experimentally observed fringe profiles of an imprinted microlens sample at wavelengths of 406 nm (A), 520 nm (B), and 635 nm (C); (D), (E), and (F) show 3D model fits of the fringe profiles, based on the 3-component refractive index vs imprint fraction simulation, for imprinted microlenses at wavelengths of 406 nm (D), 520 nm (E), and 635 nm (F); (G), (H), and (I) show 2D cross sections of the model fits and experimental data shown in Figures (A) through (F); (J) A plot showing how refractive index varies with porosity according to the 3-component Bruggeman approximation; (K) 3D image of the index profile of the imprinted lenses ; (L) 2D cross section of an imprinted lens showing the imprint topology as well as the resulting porosity profile; (M) simulated gradient refractive index profiles of the imprinted microlens at the three test wavelengths

The extracted refractive index profile can be seen in Figure 15 K and M, and is found to match a hyperbolic secant GRIN profile of the form:

$$nr = C_0 \operatorname{sech}(\alpha r) + n_0 \quad (22)$$

Where n is the refractive index at radius r from the center of the microlens, n_0 is the refractive index of the film prior to imprint, and C_0 and α are gradient parameters [90]. The hyperbolic secant fit of the refractive index profile can be seen in Figure 16 below.

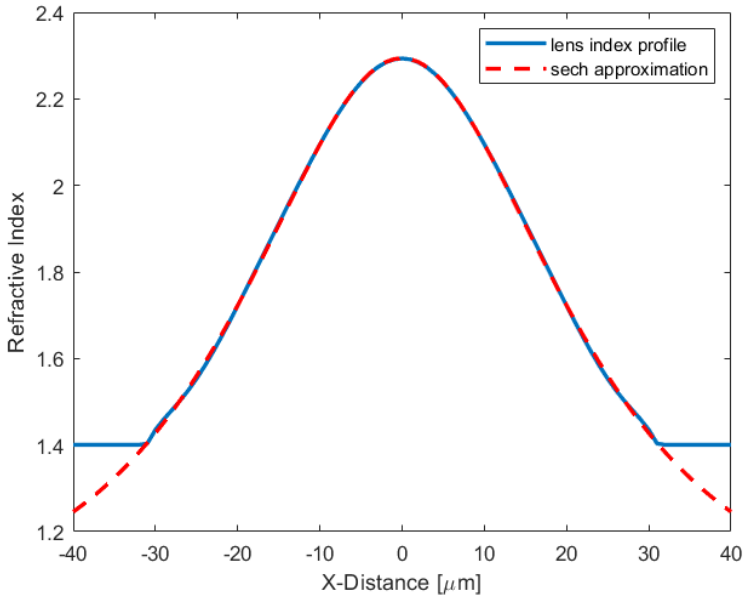

Figure 16. A graph of the simulated microlens index profile along with a hyperbolic secant fit

3.2 NIRI Microlens Performance

Following the chemical mechanical polishing and liftoff processes, we verified the wavefront-shaping capabilities of the planar GRIN profiles. As shown in Figure 17 A through C, the NIRI patterned flat optics are predicted to behave as focusing microlens arrays. Each flat GRIN lens imparts a phase profile approximated by the following formula:

$$\phi r = \frac{2\pi}{\lambda_0}\Delta nrt = \frac{2\pi}{\lambda_0}C_0 \text{sech}\,(\alpha rt) \qquad (23)$$

Where ϕ is the phase imparted by the microlens at distance r from the lens profile's center, λ_0 is the incident wavelength in a vacuum, Δn is the index contrast, and t is the thickness of the GRIN film, indicated in Figure 17 C. This indicates that the total phase coverage and focusing power of

the lens are dependent on the index contrast Δn as well as the final polished film thickness t. The thickness dependency is confirmed by the finite difference time domain (FDTD) simulations in Figure 17 A and B. As can be observed from these two simulations, a thickness change of 250 nm drastically changes the focal distance and full-width half max of the GRIN lenses. Assuming $\Delta n \approx 0.75$ and $t = 320$ nm in the experimentally fabricated GRIN microlens array, the transmitted phase coverage in the visible region is on the order of π radians. Finite difference time domain (FDTD) simulations of this geometry and refractive index profile, shown in Figure 15 M, predict focusing an incident plane-wave to a full width half-maximum (FWHM) of ~12 μm at a focal length near ~1.1 mm at λ_0 = 635 nm.

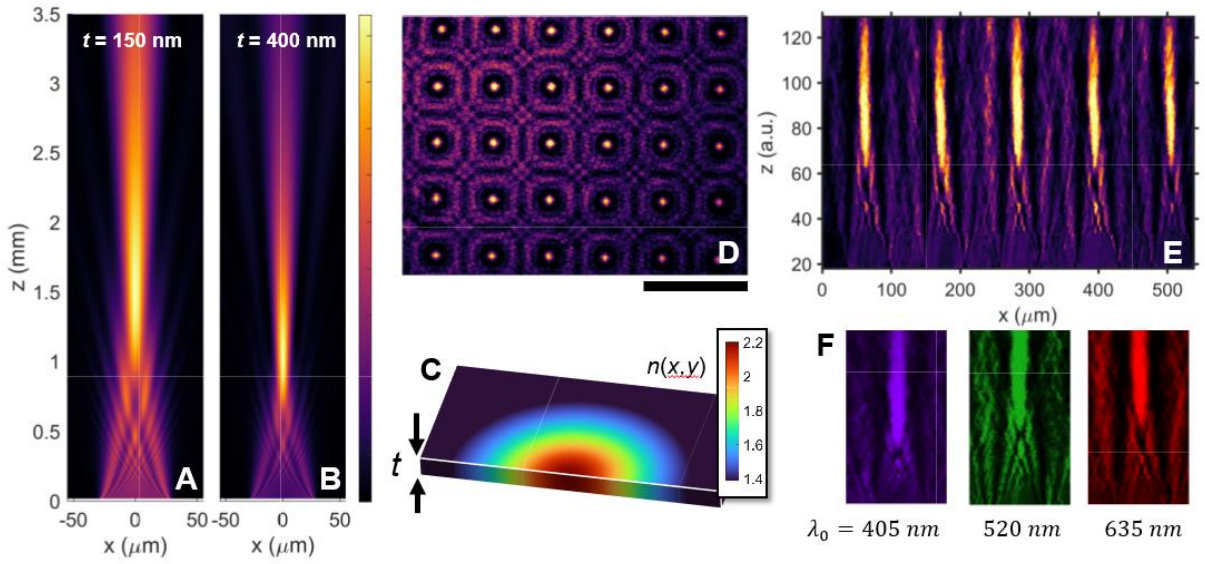

Figure 17. FDTD simulation of the flat GRIN lens operating at 635nm for planar thicknesses: (A) t = 150 nm or (B) t = 400 nm. (C) Illustration of the flat GRIN lens characterized with patterned index profile $n(x,y)$ and film thickness t. (D) Experimental image of 635 nm light focusing after transmission through a ~320 nm thick NIRI patterned GRIN microlens array (sample from Figure 14 C), and (E) corresponding z vs. x cross-section aggregated from a captured video, and (F) z vs. x cross-section demonstrating wavefront shaping at visible wavelengths 406 nm, 520 nm, and 635 nm.

To test the wavefront shaping abilities of the fabricated microlenses, we shine a collimated, planar wavefront from a multi-channel coupled laser source (Thorlabs MCLS1 4-Channel Laser

Source) through the GRIN microlens film. Figure 18 shows the measurement setup used to capture the output wavefront from the lenses. Scanning in the z-dimension is performed by recording a video as the flat-optic is manually translated along the z-axis relative to the imaging objective. Video scans are then post-processed to aggregate the video frames and construct a 2D cross-section, shown in Figure 17 E. We determine the full-width-half-maximums of the lenses by taking 2D cross-sections of pixel intensity values across multiple microlenses over all the relevant video frames. Figure 17 D shows the video frame where the full width half maximum of the output focal point is minimized for an input wavelength of λ_0 = 635 nm, indicating the microlenses are in focus.

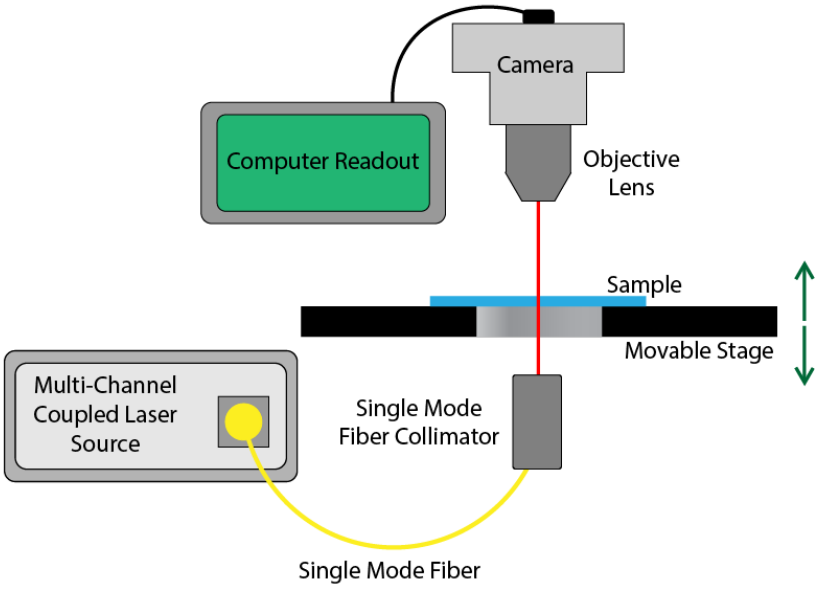

Figure 18. Diagram of the planar GRIN microlens testing setup

The measured full-width-half-max for the video frame in Figure 17 D was 14.33 μm for λ_0 = 635 nm. Similar measurements of different video captures of this sample at the same incident wavelength yielded similar FWHM results, ranging between 13.35 μm and 15.21 μm. Video scans were also captured for illumination wavelengths λ_0 = 406 nm and λ_0 = 520 nm, both of which

exhibited similar light focusing behaviors as indicated in Figure 17 F. The exact focal points of these lenses cannot be determined from the scans due to the uneven, manual nature of the z-translation in this setup, but the shapes of the simulated and experimental focal cross sections, shown in Figure 17 A and B and Figure 17 D and F respectively, are visibly very similar. This confirms the presence of a hyperbolic secant index profile realized on the fabricated lenses.

An issue that affects the quality of the video footage is the presence of wrinkles and microcracks in the pSi film containing the microlenses following liftoff onto the transparent substrate. Any wrinkles or microcracks in the sample present in a video frame scatter light from the incident wavefront, negatively impacting the clarity of adjacent microlenses. This is likely due to the strong optical anisotropy of porous silicon as well as the wavelength or super-wavelength scale of the cracks and wrinkles. The thickness of the glass cover slide used as a transparent substrate for the microlens array was ~140 μm and its transmittance at 635 nm was measured to be around ~91%. The transmission efficiency of the GRIN microlens array was measured to be ~74% as normalized to a transparent glass cover slide and is limited by absorption in the ~5 μm thick mechanical support layer etched beneath the NIRI patterned film. Figure 19 shows the transmission of this support layer as well as extrapolated transmission efficiencies for thinner support layers between 1 μm and 320 nm in thickness. These extrapolations demonstrate that a thinner support layer can drastically increase microlens transmission efficiency to > 95% in the visible range. Overall, the results of the various NIRI microlens tests indicate the successful realization of a high index contrast, truly flat GRIN-optic with a smoothly varying (non-discretized) index profile and subwavelength thickness operating at visible frequencies.

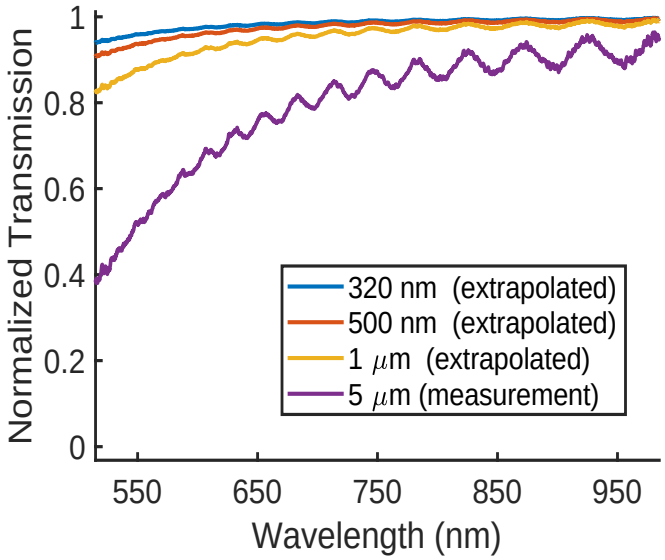

Figure 19. Measured transmission efficiency, normalized to the transmission of a microscope glass slide, of the lifted-off porous silicon film carrying the flat NIRI microlens array. Attenuation is dominated by visible light absorption of silicon in the ~5 micron thick mechanical support layer. The actual transmission efficiency for thinner layers, including the 320 nm thick NIRI patterned layer can be significantly higher.

CHAPTER 4

NANOIMPRINTING REFRACTIVE INDEX: OPTICAL WAVEGUIDES

4.1 Imprinted Optical Waveguide Fabrication

In addition to patterning GRIN profiles we utilized NIRI to pattern digital refractive index patterns $n(x,y)$ according to the procedure outlined in Figure 20. The porous silicon films used to form the waveguides are fabricated to the same specifications and using the same equipment as the porous silicon films used to form the GRIN microlenses in the previous chapter. The p-type (1 0 0) silicon wafers are placed in the etch cell, pictured in Figure 12, and etched with a current density of 55.1 for 34 seconds. This etch recipe results in a ~1.1 to ~1.2 μm thick film with a ~75% starting porosity. NIRI is performed using a 2.59x3.59 mm area solid silicon stamp containing waveguide ridges of various widths ranging from 2 μm to 0.5 μm, shown in Figure 21 B. Appendix A contains a more detailed account of the imprinting methods. As shown in the artistic rendering of the waveguide stamp in Figure 21 A and the microscope images of the imprinted pattern in Figure 21 C, in the regions between each waveguide ridge, the stamp pattern is filled with dummy pillar arrays. The purpose of these arrays is to increase the overall surface area of the stamp and to suppress long range pattern density variations which could lead to non-uniform pressures and imprint depths.

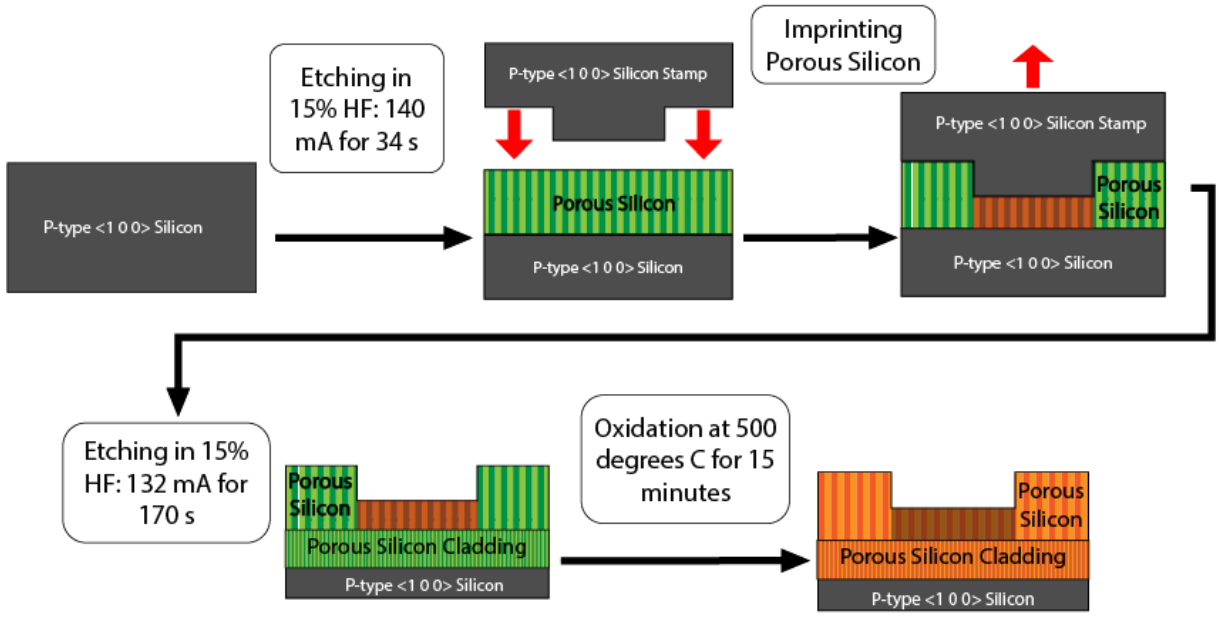

Figure 20. An artistic rendering outlining the NIRI waveguide fabrication process; following the imprinting step, a porous silicon lower cladding layer was added, and the sample was lightly oxidized, reducing loss; The darker sections indicate areas of the porous film that have been densified

The waveguide stamps were fabricated by Ivan I. Kravchenko at Oakridge National Laboratories. A four-inch Si wafer was coated in a 250 nm thick layer of ZEP520A resist and exposed to the stamp pattern using a Jeol 9300FS electron beam lithography system. Following exposure, the wafer was developed using a standard Xylenes developer and plasma-based de-scumming process. The desired etch depth was larger than what could be achieved through a single e-beam lithography step, so the surface of the resist on the wafer was coated with a 10 nm layer of Cr and treated in a hot NMP bath to generate a Cr mask pattern. The wafer with its Cr mask was subsequently etched to the desired depth using an Oxford plasma etcher, and then the Cr mask was removed using a wet Cr etchant. Finally, the residuals on the wafer were removed using oxygen microwave plasma exposure.

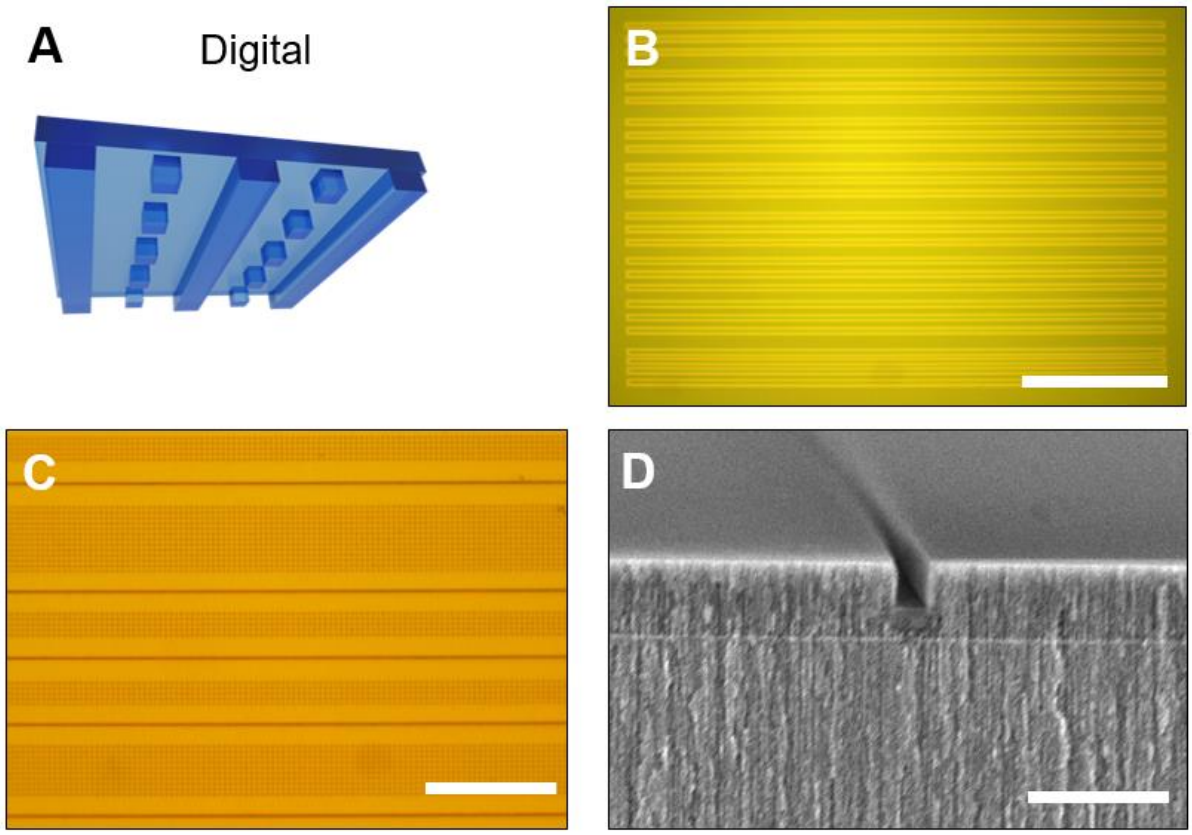

Figure 21. (A) An artistically rendered closeup of a stamp used to fabricate the digitally-patterned NIRI waveguides, (B) An optical microscope image of one of the waveguide stamps showing the arrangement of all of the waveguide ridges; the light grey areas around the outside of the stamp are comprised of dummy pillar arrays (scale bar 500 μm), (C) an optical microscope image of an imprinted waveguide sample (scale bar 100 μm), (D) a cross-sectional SEM image of an imprinted waveguide following the secondary electrochemical etch to add low index waveguide cladding (scale bar 2 μm).

The resulting etch depth of the stamp features was ~1 μm. The stamp depth was selected to be deeper than the maximum imprint depth of ~900 nm assuming P_0 = 75% porosity and 1.2 μm starting film thickness. This ensures that the stamp only contacts with the substrate and densifies areas defined by the digital pattern, while leaving the background index n_0 unmodified. When the stamp etch depth is insufficient, as was the case in earlier stamp prototypes, pieces of the porous silicon film can become detached from the substrate and adhere to the stamp during imprint. Compared to fused silica, silicon has a much lower compressive strength and is much more subject

to fracturing. Consequently, the stamp lifetime was significantly reduced to a maximum of 15 imprints. Additionally, unlike the fused silica microlens stamp, the silicon waveguide stamps could not be cleaned using sonication in isopropyl alcohol, as this was found to degrade the binary ridge features of the stamp. This made the silicon stamps more susceptible to dirt and debris that impacted the imprint quality.

Following imprint, we return the sample to the etch cell to etch a porous silicon cladding layer below the waveguides to improve confinement. The current density used in this step is 52 mA/cm^2 applied for 170s, yielding a cladding layer of thickness ~5 μm. This current density is lower than in the first etch phase to avoid structural collapse of the porous skeleton. The lower cladding layer is visible in the cross-sectional SEM image in Figure 21 D, and it can be observed that the second etch did not interfere with the densified waveguide region and that the etching resumes unimpeded by the densified porous film above, confirming that film integrity is retained after secondary anodization. The patterning of the waveguide in Figure 21 D also demonstrates that NIRI is capable of patterning sub-micron features while imprinting with >1:1 aspect ratio. While prior direct imprinting work has demonstrated a topographic direct imprinting resolution <100 nm [60], in practice we expect the minimum patterning resolution to depend on factors such as maximum aspect ratio and imprint depth. In this work we successfully imprinted line features as small as ~350 nm in width to a high compression regime, i.e. $C \geq 60\%$ where $\Delta n \geq 0.8$, for a maximum aspect ratio of ~2.75:1.

As can be seen from the optical microscope image of the imprint in Figure 21 C, there was a structural color change in the imprinted areas from the yellow of the non-imprinted areas to a dark reddish-brown. This, along with the relatively high imprint pressures used in fabrication indicates a large imprint fraction, and consequently a large refractive index contrast. The large refractive

index contrast is confirmed by Figures 22 A and D, which show scanning electron microscope images of the cleaved facet of a ~2-μm and a ~0.5-μm-wide NIRI imprinted waveguide respectively. For Figure 22 D, it was determined that the non-imprinted film height is 1.1 μm and the imprinted film height is 0.328 μm, so the imprint fraction in this case is 0.702. As for the waveguide in Figure 22 A, the non-imprinted height is 1.09 μm, and the imprinted height is 0.294 μm, so the imprint fraction is 0.730.

According to the film compression vs. porosity model in Figure 10 C, the porosity of the imprinted film should be very close to 0 for both imprints: 0.075 and 0.161 for the waveguides in Figure 22 A and D respectively. This is confirmed by the absence of visible pores in the imprinted areas in Figures 22 A and D. According to the 3-component refractive index vs. imprint fraction model, the refractive indices of the waveguides in Figures 22 A and D should be 2.31 and 2.19 respectively. The non-imprinted pSi film has been characterized to have an index of 1.287, so the imprints in Figures 22 A and D would correspond to index differences of Δn = 1.023 and Δn = 0.899 respectively. The index profiles for both waveguides, modelled in Lumerical Mode, are shown in Figures 22 B and E. The high refractive index differences, bode well for waveguide confinement. Previous works indicate that a compression this close to the limit of 0.75 would cause the silicon skeleton in the imprinted area to become brittle and dislodge, but this has, so far, not been observed in the imprinted waveguide samples [82]. This is likely due to the fact that the waveguide samples in this study were briefly thermally oxidized for 15 minutes at 500°C prior to testing. The volumetric expansion from the formation of the native SiO2 oxide during oxidation likely locked the potentially loose material into the film.

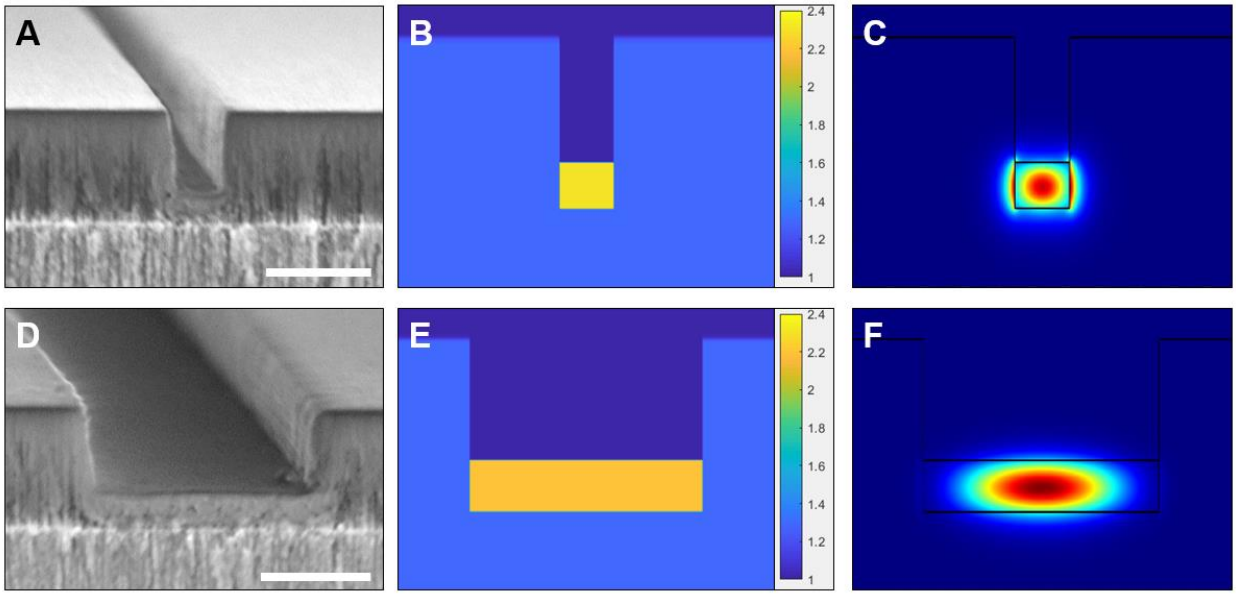

Figure 22. (A) A scanning electron microscope image of the cross-section of a ~0.5 μm wide imprinted waveguide at 4.0k magnification. (B) A simulated index profile of the ~0.5 μm waveguide based on the cross section and the 3-component imprint fraction vs. index approximation (C) a mode simulation of the primary TE mode for the ~0.5 μm waveguide at λ = 1310 nm (D) A scanning electron microscope image of the cross-section of a ~2 μm wide imprinted waveguide at 11.0k magnification (E) A simulated index profile of the ~2 μm waveguide based on the cross section and the 3-component imprint fraction vs. index approximation (F) a mode simulation of the primary TE mode for the ~2 μm waveguide at λ = 1310 nm

4.2 NIRI Waveguide Performance

Following the thermal oxidation, we experimentally characterized NIRI patterned waveguides operating in the O-band from 1260 nm - 1360 nm. To enable input/output coupling, the waveguide patterns were cleaved into ~1 mm long waveguide segments with exposed waveguide edge facets as shown in Figure 22 A and D. The cleaving step significantly reduced the yield of usable waveguide samples, as the cleaved samples were often left with edge facets that were not perpendicular to the upper face of the sample, making coupling more difficult. The cleaving process also introduced an additional opportunity for physical damage, such as scratches or chips, to the porous silicon film, which rendered a number of waveguide samples unusable. In these cleaved waveguide samples, in-plane optical confinement is achieved by the laterally patterned

index profile while out-of-plane confinement is provided by the index contrast between the imprinted core and the low index cladding layer formed by the second anodization step mentioned in the previous section. The mode simulation (Ansys Lumerical), shown in Figure 22 F, indicates that the fundamental quasi-TE polarized mode is well confined to the waveguide core.

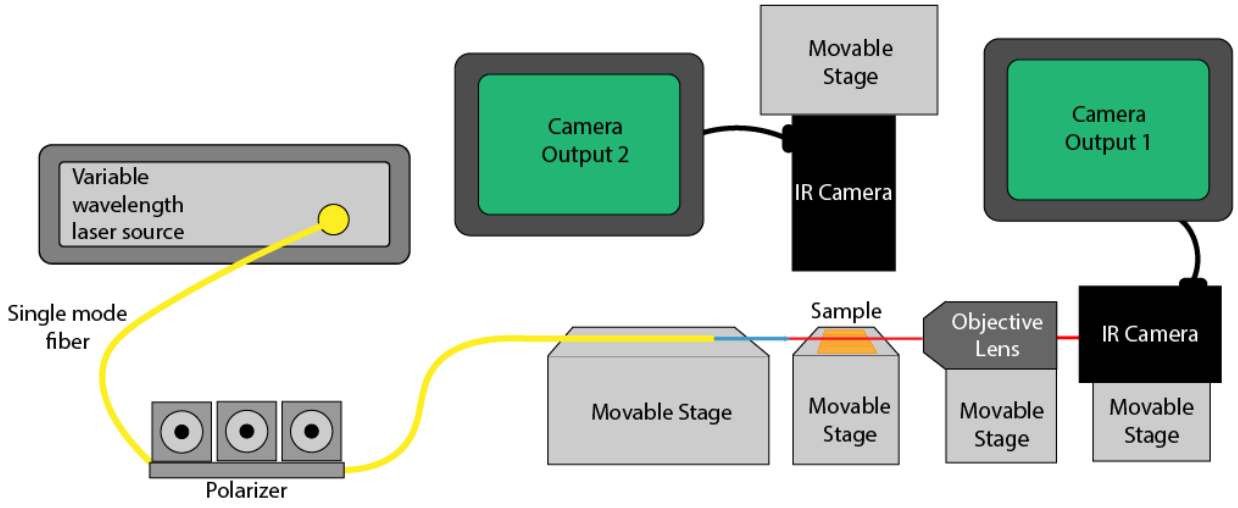

Figure 23. Waveguide characterization setup

The cleaved waveguide samples are characterized using the setup shown in Figure 23. We perform fiber-to-chip coupling using a tapered lensed fiber with a ~2.5 μm spot diameter and ~14 μm working distance (OZ Optics), which we align to the chip using a high precision XYZ alignment stage (Thorlabs NanoMax) with the aid of top and side-view infrared cameras (Hammamatsu C2741). The strong waveguide confinement and mode mismatch with the input light source leads to an estimated ~10 dB coupling loss between the input fiber and waveguide. In the future improved coupling efficiency could be achieved by implementing a mode convertor or using NIRI to pattern a grating coupler to facilitate efficient out-of-plane coupling. Such a device could be engineered by either digitally patterning a binary refractive index profile or by engineering a gradient or analog index profile to optimize edge or grating coupler efficiency [6], [45]–[47].

A microscope objective (Mitituyo 50x M Plan APO NIR) and a tube lens (Navitar 12x Zoom Infrared Lens Tube) are used to focus the light from the waveguide's output onto an IR camera lens, as shown in Figure 23 above. A free-space polarizer placed between the objective lens and lens tube is used to verify quasi-TE polarization, which is controlled by the polarization controller (Thorlabs 3-paddle) placed between the laser source and the sample. The scattered light intensity is measured by averaging top-down images taken at wavelengths from 1260 nm to 1360 nm (Santec TSL-550). Imaging is calibrated by capturing top-down images for input power settings ranging from 10 dBm to 1 dBm at intervals of 1 dBm. Image processing is performed in MATLAB to determine the waveguide propagation losses. One of these top-down images can be seen in Figure 24 C below. From visual inspection of this image, it is obvious that the scattered light intensity decays as it propagates down the waveguide. The data extracted from image processing of this waveguide can be seen in Figure 24 E. The waveguide loss was found to be 8.103 ± 0.245 dBm/mm using the image processing method. This value is comparable to other reports of mesoporous silicon waveguides prepared by lithography and RIE in low resistivity p-type silicon [91], [92].

Although non-negligible optical scattering is visible in the infrared camera, the dominant loss mechanism is attributed to free-carrier absorption of the p-doped silicon skeleton. The (1 0 0) silicon wafers used to create the waveguides have an acceptor concentration N_A = 3.2E18 to 8.5E18, which we will assume is the same for the imprinted waveguides. This value can be used along with the coefficients and linear regression formulas to describe how the absorption coefficient and refractive index of silicon changes with carrier concentration, as derived in a paper by Nedeljkovic et al [93]. The formula derived for absorption coefficient is as follows:

$$\Delta\alpha(\lambda) = a(\lambda)\Delta N_e^{b(\lambda)} + c(\lambda)\Delta N_h^{d(\lambda)}$$

(24)

Here, ΔN_e and ΔN_h are the electron and hole concentrations due to doping and *a*, *b*, *c*, and *d* are wavelength-dependent coefficients. In this case, due to the strongly p-type doping, the term containing ΔN_e is negligible and can be disregarded. Using this formula, the predicted free-carrier absorption coefficient of silicon at $\lambda_0 = 1.3$ μm is estimated to be between 14.3 cm^{-1} and 42 cm^{-1} for a silicon loss coefficient between 6 – 18 dB/mm [93]. Thus, a waveguide confinement factor in silicon near ~0.5 is sufficient to attribute the majority of the observed propagation loss to free-carrier absorption rather than scattering loss. We also note that our measured propagation loss is consistent with other reports of mesoporous silicon waveguides prepared from low resistivity p-type silicon [94]. In the future, losses could be improved by lowering the free-carrier concentration to near intrinsic values, for example by compensation doping or by synthesizing mesoporous films by alternative processes such as metal-assisted chemical etching which are compatible with high resistivity silicon [78]. Alternatively, and as demonstrated in this work, the waveguide loss can be improved by oxidizing the waveguide from mesoporous silicon into mesoporous silica.

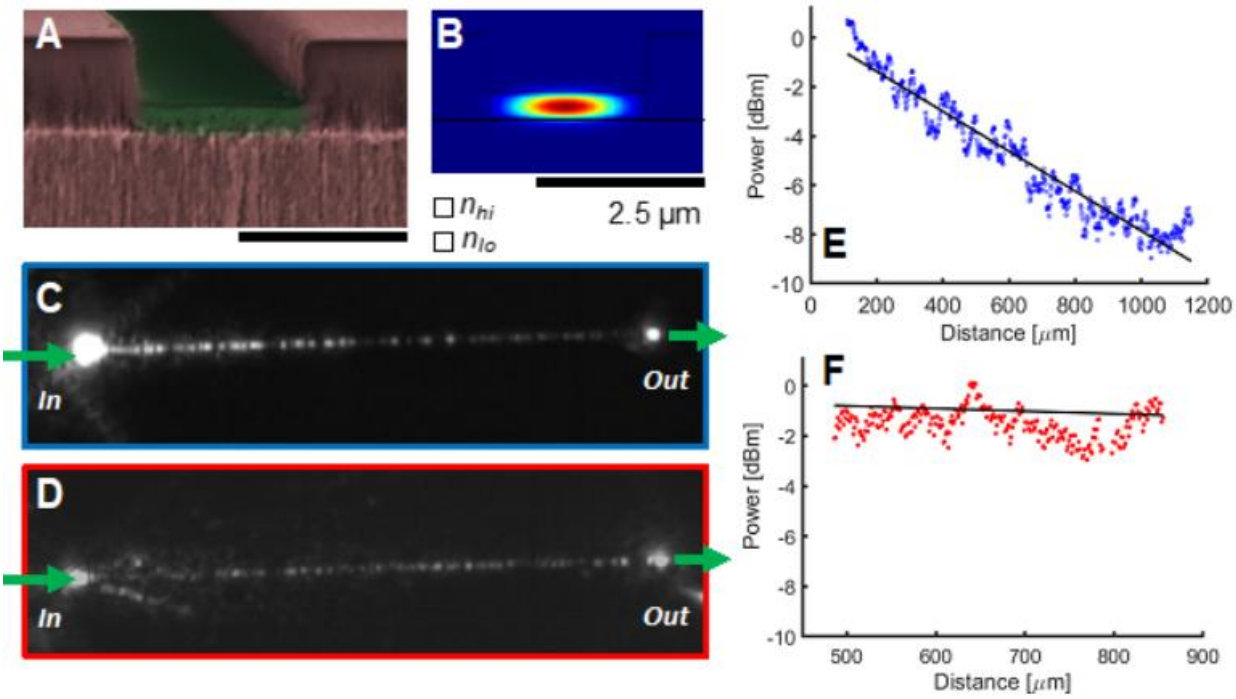

Figure 24. (A) SEM image of a 2-µm-wide imprinted waveguide facet (2 µm scale bar), (B) Lumerical MODE simulation based on the facet in (A) and showing the dominant TE mode at a wavelength of 1310 nm, (C) top-down IR image of a 2µm wide, non-oxidized waveguide guiding light at an input wavelength of 1300 nm, (D) A top-down view of a different 2-µm-wide waveguide after full thermal oxidation guiding input light at a wavelength of 1300 nm, (E) Graph of the power loss over the non-oxidized waveguide in (C) that shows a waveguide loss of 8.103 ± 0.245 dBm/mm, (F) Graph of the power loss over the oxidized waveguide in (D) that shows a waveguide loss of 1.1054 ± 1.010 dBm/mm.

Following the fabrication procedure shown in Figure 20 and cleaving, we thermally oxidize some of the samples at 900°C for 24 hours in order to fully oxidize the silicon skeleton. In addition to eliminating free-carrier absorption, this process modulates the refractive index contrast of the waveguide which is bounded to material indices between air (n = 1) and SiO_2 (n = 1.45). Based on fitting the reflectance spectra of oxidized mesoporous silicon thin-film witness samples, we estimate the high and low refractive indices of our mesoporous silica waveguides to be $n_{hi} \approx 1.38$ and $n_{lo} \approx 1.15$. An example of one of these fully oxidized samples can be seen in Figure 24 D. The sample shown in Figure 24 C was also fully oxidized after testing, but stopped waveguiding following oxidation, possibly due to the volumetric expansion of the Si skeleton as it oxidized,

changing the waveguide geometry. The sample in Figure 24 D was a different sample that was found to waveguide strongly following oxidation.

As can be seen from even a visual comparison between Figures 24 C and D, there was much lower loss along the oxidized waveguide, as the scattering within the oxidized waveguide is relatively constant in intensity between the source (left) and the output (right). This was confirmed by the image processing procedure used to calculate the waveguide loss, the results of which can be seen in Figure 24 F for the oxidized waveguide. The loss was found to be ~1.1 ± 1 dB/mm. Due to the lower propagation losses and the influence from light scattering at the facets, our IR imaging-based analysis of oxidized samples was limited to the middle ~500 μm portion of the waveguide (Figure 24 F), limiting the measurement accuracy to ± 1 dB/mm. In future work, measurements of longer mesoporous silicon waveguides can be used to estimate the waveguide loss with reduced uncertainty. Based on prior reports regarding mesoporous silica [94], we anticipate surface-scattering limited losses below 1 dB/cm in the infrared and volume-scattering limited losses below 5 dB/cm in the visible should be feasible.

CHAPTER 5

CONCLUSION AND OUTLOOK

5.1 Conclusion

We demonstrated two proof-of-concept optical devices fabricated using the nanoimprinting of refractive index (NIRI) process. We successfully designed, fabricated, and characterized a planar GRIN microlens array and several digitally patterned optical waveguides. We achieved a flat, subwavelength-thickness porous silicon microlens with an approximate transmitted phase coverage of π in the visible region and an overall transmission of ~74%. These microlenses demonstrated distinct wavefront-shaping behavior at visible wavelengths of 406 nm , 520 nm, and 635 nm consistent with their hyperbolic secant phase profiles and with the results of corresponding FDTD simulations. The focal length of these lenses at 635 nm is estimated to be ~1.1 mm, and the FWHM of the focal point was measured to be ~14 μm.

We also demonstrated digitally patterned waveguides fabricated using the NIRI process. Our 2-μm-wide waveguides successfully guided light in the O-band from 1260 nm - 1360 nm. We characterized the waveguide loss using data from IR imaging systems, which indicated an initial propagation loss of 8.103 ± 0.245 dBm/mm. We determined that the majority of this propagation loss was due to free-carrier absorption rather than scattering loss due to the roughness of the waveguides using formulas developed by Nedeljkovic et al [93]. We confirmed this by determining the propagation loss of a fully oxidized waveguide sample, which we found to be 1.1054 ± 1.010 dBm/mm, an 8-fold reduction from the non-oxidized waveguide. Through the fabrication and demonstration of these two types of devices, we have confirmed the ability of the nanoimprinting of refractive index (NIRI) process in performing both gradient and digital index patterning of mesoporous silicon.

5.2 Outlook

Unlike flat-optic technologies based on discretized local phase elements or meta-atoms, NIRI enables truly continuous control over the phase profile. The NIRI process offers effective index patterning and performance similar to that found in subwavelength gratings, even at wavelengths as low as 406 nm, which is extremely difficult to achieve in subwavelength gratings using conventional manufacturing techniques. The devices fabricated in this research represent a proof-of-concept of NIRI for use in optical device fabrication. That being said, there is ample room to improve the aforementioned NIRI-fabricated devices and procedures. For instance, the specific planarization process used in fabricating the microlenses tended to be uneven, leaving a gradient over the sample. Additionally, the polishing process was not well-controlled, so getting a precise film height was relatively difficult to accomplish. As discussed in chapter 3.2, the film thickness has a significant effect on the focusing characteristics of our GRIN microlenses, so it is important to tightly control film thickness. We also need to control and measure the vertical height of the microlens sample during transmission tests to experimentally determine the microlenses' focal length more precisely. It will also be worthwhile to implement flat optical devices with full 2π phase control using the NIRI process, as those in this research only demonstrated phase control of $\sim\pi$, which is insufficient for many planar optical devices. As for the waveguides, it will be necessary to further investigate and improve the propagation loss. In order to gain a better understanding of the waveguide loss, we will need to measure longer waveguide samples, particularly for the oxidized waveguides, where scattering from the facets is more prominent.

As demonstrated in this work, the NIRI process is promising for device fabrication. The combination of high index contrast and subwavelength resolution offers the prospect of enabling novel GRIN designs which are otherwise challenging to achieve by other methods. In future work,

we envision NIRI could leverage 3D surface patterning to define custom reusable stamps to fabricate fully customized digital or analog refractive index profiles. In addition to wavefront shaping, NIRI can simultaneously modulate amplitude by leveraging Fabry-Perot interference. Consideration of the superstrate and substrate properties are therefore also important for controlling the local Fresnel transmission/reflection coefficients. These properties could also be modified using a variety of techniques such as polymer infill of the pores. Another consideration in future work is the birefringence of mesoporous silicon. In the present case, (100) derived mesoporous silicon exhibits uniaxial anisotropy and a polarization independent response when illuminated at normal incidence. For planar waveguide applications or oblique incidence metasurface applications however, the effective refractive index is polarization dependent which provides an additional consideration and prospective design tool for polarization diverse applications [71]. Similarly, polarization dependence could be achieved in normal incidence metasurfaces for (110) derived mesoporous silicon which exhibits biaxial anisotropy [95]. In such cases, we anticipate the magnitude of the birefringence to be modulated by film compression since the anisotropy is dependent on the pore morphology. For certain prospective applications, such as NIRI based photonic integrated circuits, conversion to mesoporous silica from mesoporous silicon will also affect the birefringence.

APPENDIX

Appendix A: Imprinting Methods

Some of the stamps used for the imprinted waveguides are shown below in Figure S1.

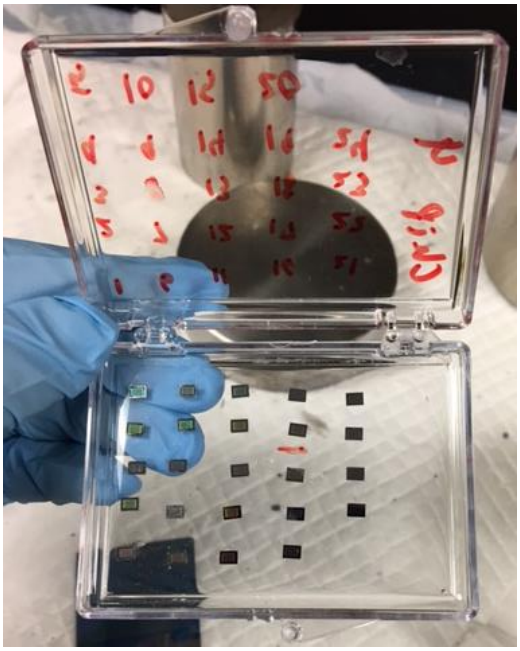

Figure S1. Imprinted waveguide stamps

Before each imprint, the stamp being used is rinsed in isopropyl alcohol, as shown in Figure S2. The waveguide stamps could not be sonicated because the sonication would break the delicate ridges on the stamps. Following the brief rinse, the stamps are allowed to air dry.

Figure S2. Waveguide stamp cleaning process

To prepare the porous silicon sample to be imprinted, it is rinsed in isopropyl alcohol and dried using pressurized air. After this initial rinse, a backing of Scotch tape is added to the back of the sample such that there are no bubbles in the tape, as shown in Figure S4. The addition of the tape was found to decrease the likelihood of the sample or stamp cracking during imprint, however bubbles in the tape can lead to uneven imprinting.

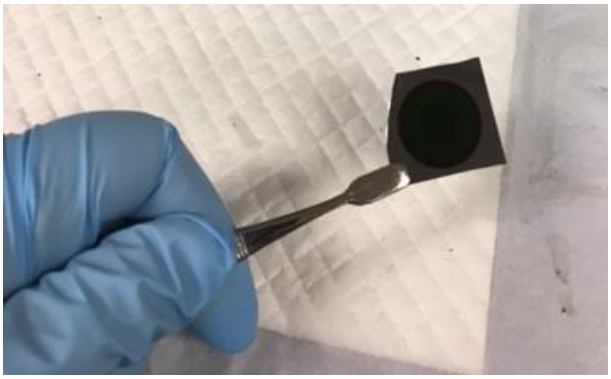

Figure S3. A porous silicon sample to be imprinted

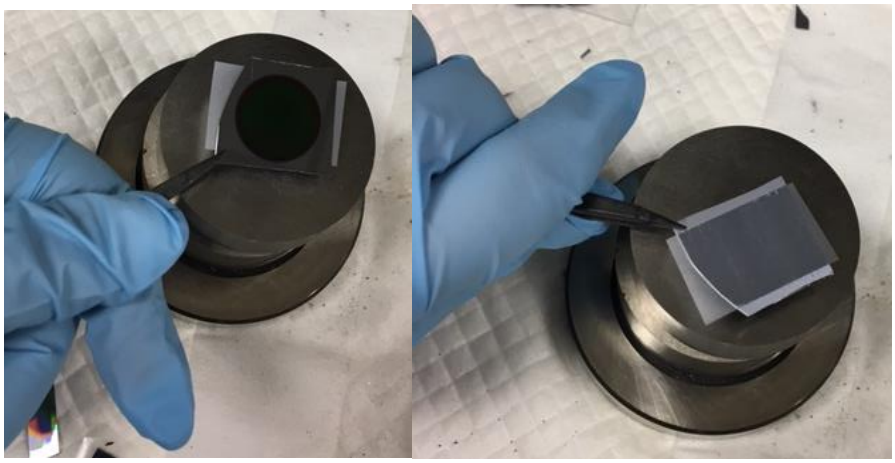

Figure S4. Front (left) and back (right) of a porous silicon stamp with its tape backing

A similar tape backing is also added to the backside of the stamp, as shown in Figure S5. This tape backing is used to secure the stamp to the sample during imprinting, ensuring that it doesn't

shift as pressure is applied. Care is taken to align the stamp to the existing cleaved crystal planes of the sample to aid in cleaving the imprinted waveguides.

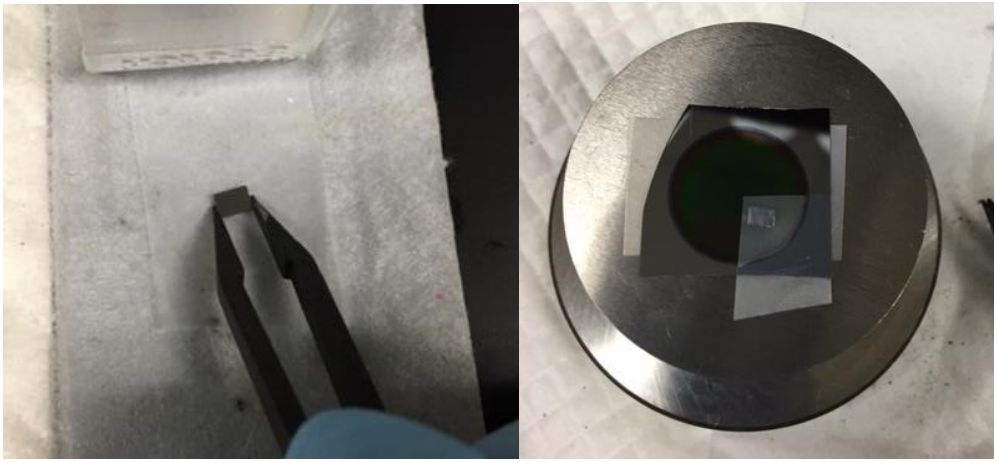

Figure S5. Stamp receiving tape backing (left) Stamp with backing mounted on the porous silicon sample (right)

Figure S6 shows a cleaved cross-section of an imprinted sample where the stamp shifted during imprint, damaging the waveguide structure.

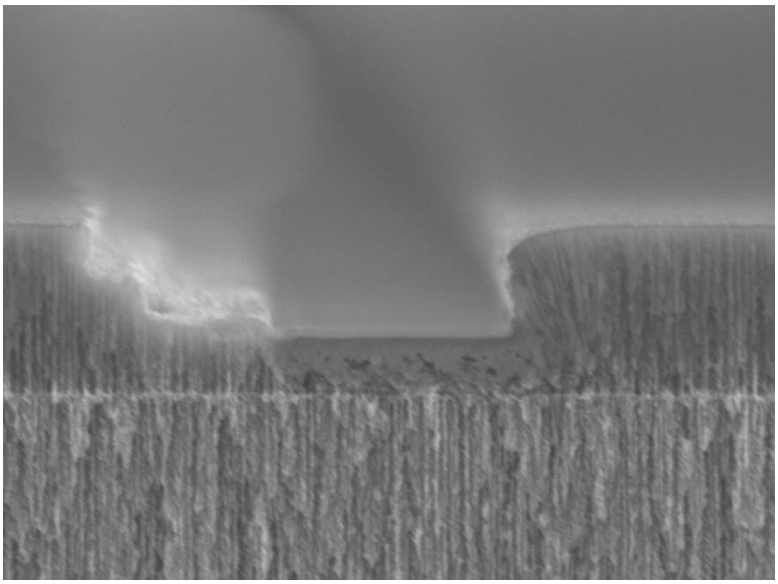

Figure S6. Scanning electron microscope image showing a cross-section of a waveguide. The damage on the left of the waveguide was caused by the stamp shifting during imprint

The stamp and sample are placed in the jig as shown in Figure S7. After this, the handle at the top of the jig is detached and the jig is placed in the hydraulic press.

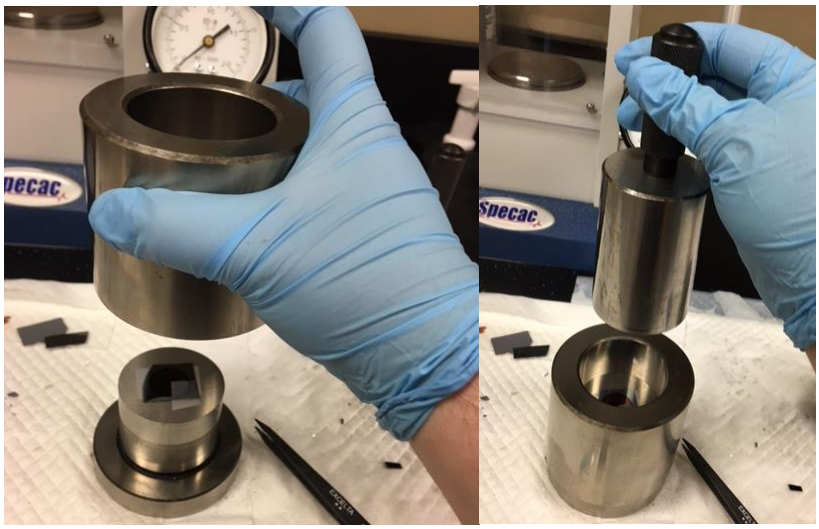

Figure S7. The porous silicon sample and stamp are placed in the jig for imprinting

The hydraulic press is operated as shown in Figure S8 after the jig is positioned appropriately. The specific pressure used for these stamps was 0.1 T. Higher pressures were found to over-imprint the porous silicon or even break the stamp or sample. Lower pressures under-imprinted the samples, which also led to unevenness in the pressure over the stamp. The pressure in the hydraulic press is held for approximately 5 seconds before it is released, and the sample is retrieved.

Figure S8. The jig is placed in the hydraulic press (left) and a pressure of 0.1 T is applied (right)

Figure S9 shows a sample after being imprinted. The stamp was removed prior to this, but some tape residue remains around the imprint. This residue has not been found to affect the quality of the imprinted pattern. Following this, the sample is once again rinsed in isopropyl alcohol.

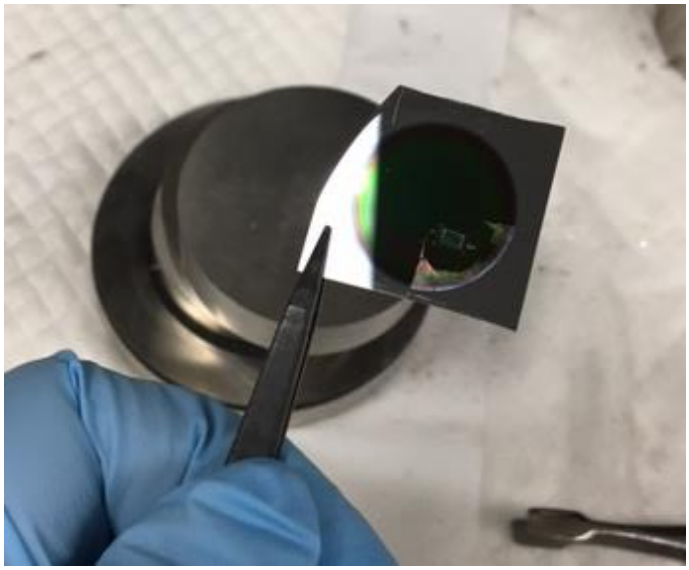

Figure S9. Porous silicon sample after imprint and stamp removal

The frequent isopropyl alcohol rinses of the sample and stamp are designed to minimize the presence of dirt in the imprints. Debris can be seen in the imprint in Figure S10.

Figure S10. Microscope image showing a waveguide imprint that has been degraded by debris

The imprinting procedure for the microlenses is similar to that of waveguides except for some minor differences. The microlens stamp was made of fused silica instead of silicon, so it could stand up to sonication. Prior to imprints, the microlens stamp is sonicated for 5 minutes in isopropyl alcohol. Additionally, the microlens stamp has a larger area than the waveguide stamp, so a higher pressure of 0.4 T is applied during imprint.

Appendix B: Polishing Methods

We used the Buehler VibroMet 2 vibratory polisher with 60 nm-diameter colloidal silica polishing solution, as shown in Figure S11.

Figure S11. Bueler VibroMet 2 vibratory polisher

We used solid stainless steel chucks as shown in Figure S12. In order to increase the weight on the sample, we stack two chucks on top of one another and secure them with tape, as shown in Figure S13.

Figure S12. Two chucks used in polishing

Figure S13. The chucks are stacked vertically (left) and secured with duct tape (right)

We then secure the sample to the bottom-most chuck using double-sided conductive SEM tape. We utilize two layers of double-sided tape rather than one to aid in removing the sample after the polishing process. The second layer of tape is applied perpendicular to the first, as shown in Figure S14, which was found to produce the optimal amount of tape contact with the back of the sample. Too much tape contact was found to cause sample breakage during removal, and too little tape contact allowed the sample to detach from the chuck in the polisher.

Figure S14. First tape layer (left) and second tape layer during backing removal (right)

Following this, we attach the sample to the tape, porous side up, and place the chucks sample-side-down in the polisher, as shown below.

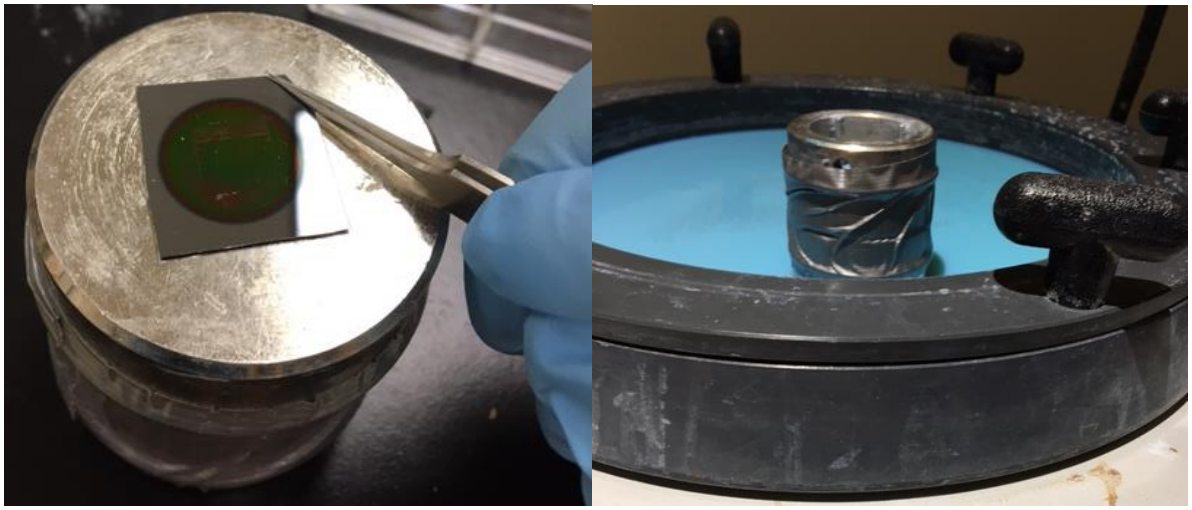

Figure S15. The sample attached to the chuck (left) and the chuck in the polisher (right)

The VibroMet polisher allows for amplitude adjustment between 0 and 100 % at intervals of 10. A setting of 70% was used to polish the samples used in testing. During polishing, the chucks do

not experience consistent planetary motion within the polisher, so to ensure even polishing, the chucks are rotated by hand periodically (at least once every 5 minutes), as shown in Figure S16.

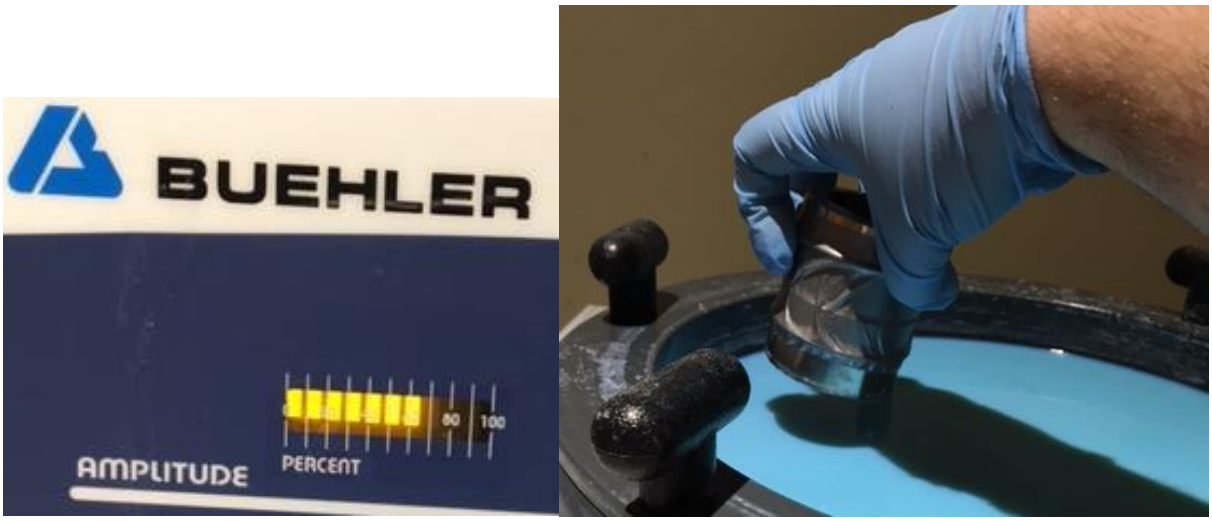

Figure S16. Correct polisher setting (left), rotation of the chuck (right)

Improper rotation of the sample led so uneven polishing, which can be seen in the samples in Figure S17.

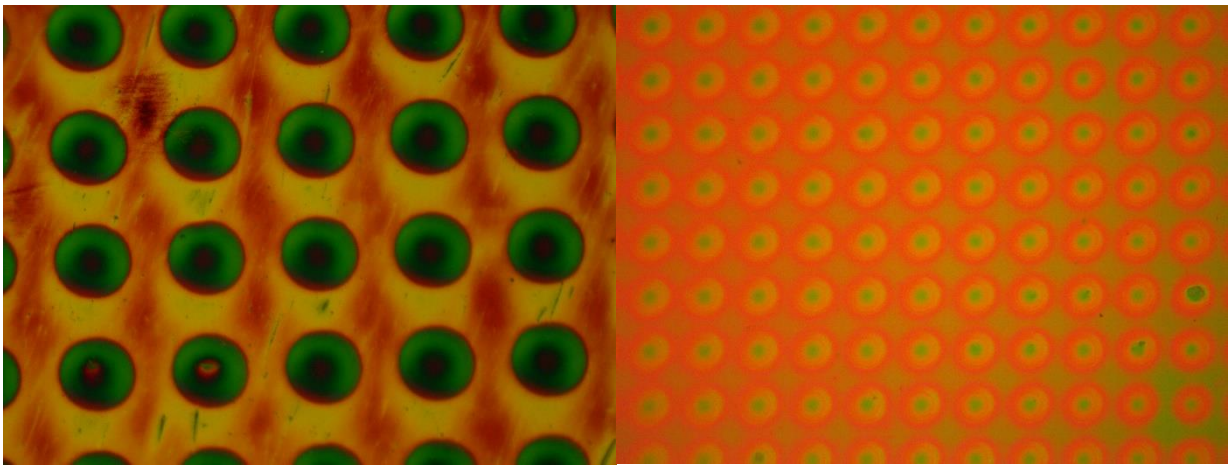

Figure S17. Microscope images showing samples with polishing gradients due to insufficient planetary rotation

After polishing has finished, the chucks are removed from the polisher, and the sample gets an initial rinse in isopropyl alcohol to remove some of the polishing solution while it is still attached to the chuck, as shown in Figure S18.

Figure S18. Initial isopropyl alcohol rinse of the polished sample

Following this initial rinse, acetone is sprayed around the edges of the sample to dissolve the double-sided tape adhesive. The porous part of the sample is kept wet with isopropyl alcohol, as shown in Figure S19. If acetone becomes lodged in the pores of the sample and dries there, the rapid temperature change that accompanies acetone's evaporation can damage the pore structure.

Figure S19. Acetone application (left), isopropyl alcohol re-application (right)

After this acetone treatment, the sample can be removed by using a thin mixing spatula to gently push back the tape and pry the sample up, as shown in Figure S20. Excessive pressure on the sample during this stage can cause it to fracture, making it ineligible for receiving a second etch treatment. After the sample is lifted off of the chuck, it is once again rinsed with isopropyl alcohol.

Figure S20. Removal of the sample from the chuck using the mixing spatula (left) and then forceps (right)

Following this rinse, the sample is submerged in more isopropyl alcohol for transport. This prevents crystallization of the remaining polishing solution on the sample.

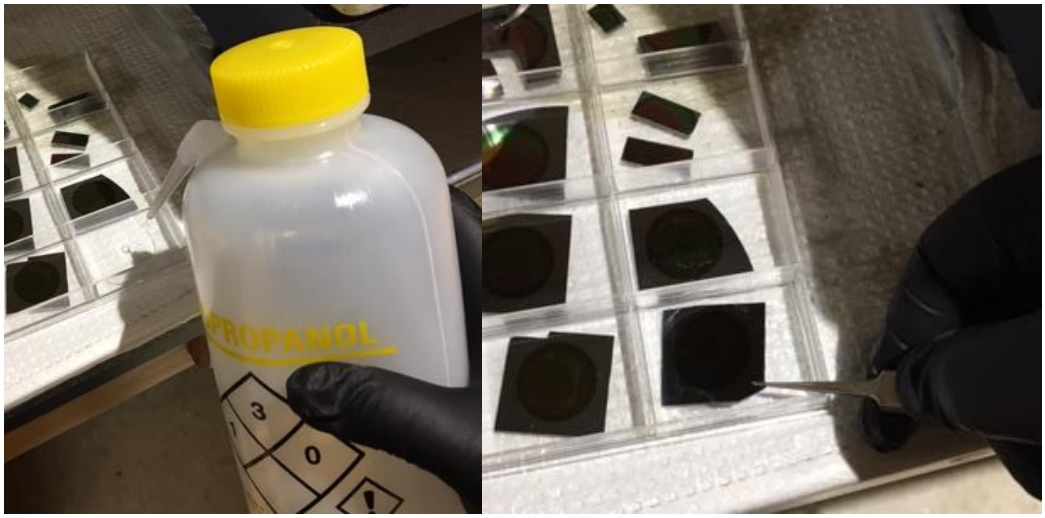

Figure S21. The isopropyl alcohol bath is prepared for the polished sample (left), the polished sample is submerged in isopropyl alcohol (right)

Another isopropyl alcohol rinse is applied to the sample before it is placed in a beaker containing just enough isopropyl alcohol to submerge it. This beaker is then placed in a sonicator set to run

for 10 to 15 minutes. After this sonication, the sample is rinsed in isopropyl alcohol and dried, completing the polishing process.

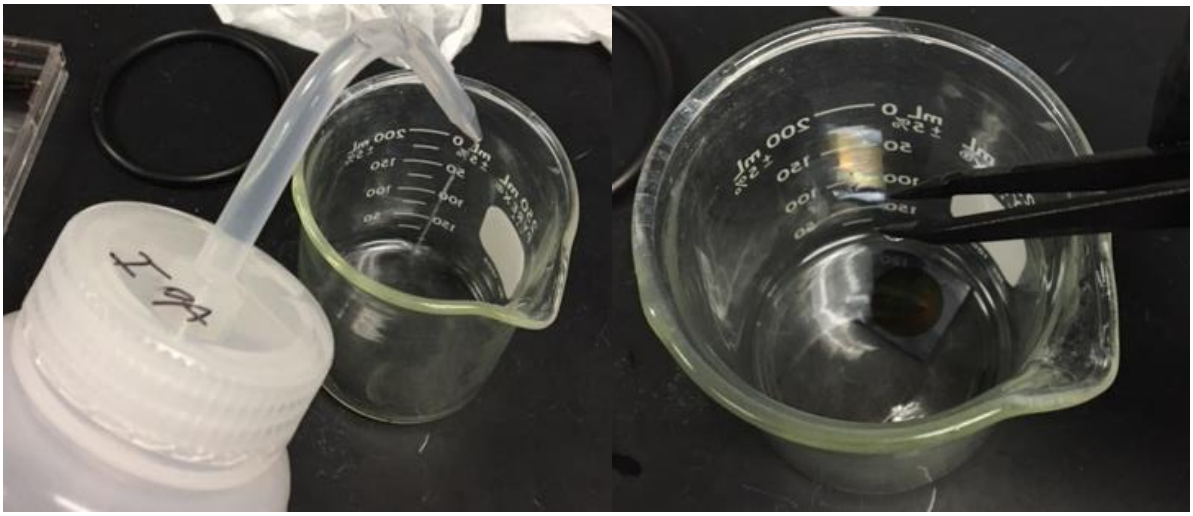

Figure S22. Isopropyl alcohol is added to a beaker (left), the polished sample is submerged in the isopropyl alcohol in preparation for sonication (right)

Figure S23. The beaker containing the polished sample submerged in isopropyl alcohol is sonicated for 10 minutes

Overall, the polishing process was highly variable, as can be seen in the graph in Figure S24 of measured polish thicknesses (based on SEM images of sample cross-sections). Several different vibratory polish settings were used, as can be observed from the chart, but we found that a setting of 7 (70% amplitude) yielded the best results for a sub-500 nm final thickness. The

variation in the sample polishing rates shown in the chart is likely due to variations in the samples themselves as well as variations in the polishing solution. Some of the sample variations likely arose during the etch process due to slight variations in the platinum wire anode position within the cell, as well as variations in the aluminum foil covering on the backplate beneath the silicon wafer. Further confirmation of these variations is in the noticeable variation in structural color of the resulting porous silicon samples, indicating variations in porosity and/or porous layer thickness. Additional variations were also likely introduced during the thermal oxidation phase because the temperature inside the thermal oxidation chamber varied significantly around the set point. This introduced different levels of oxidation to the samples, causing the more oxidized samples to have a slower polishing rate.

The polishing process introduced variations because the polishing solution was not changed between each polish. The polishing solution had a water base and tended to evaporate and densify over time. Additional deionized water was added to the solution periodically, but there was still variation in the water content of the solution. There was a slight improvement in polishing rate consistency immediately following a solution change, but this was not significant enough to warrant changing the solution after each polish. There was additional variation introduced by the initial shape and area of the samples, which were cleaved from standard 100 mm wafers. The area of these cleaved pieces of wafer was not standardized and the circular edge of the wafer introduced shape variation into the samples. It is possible that the amount of non-porous silicon surrounding the porous silicon on a sample affected the polishing rate. The primary microlens sample tested in the main study is not pictured on the chart in Figure S24, since it would need to be cleaved for measurement, and this would prevent it from being put back in the etch cell.

We calculated the thickness of this sample using reflectance data, since extrapolation from polishing data was found to be inaccurate.

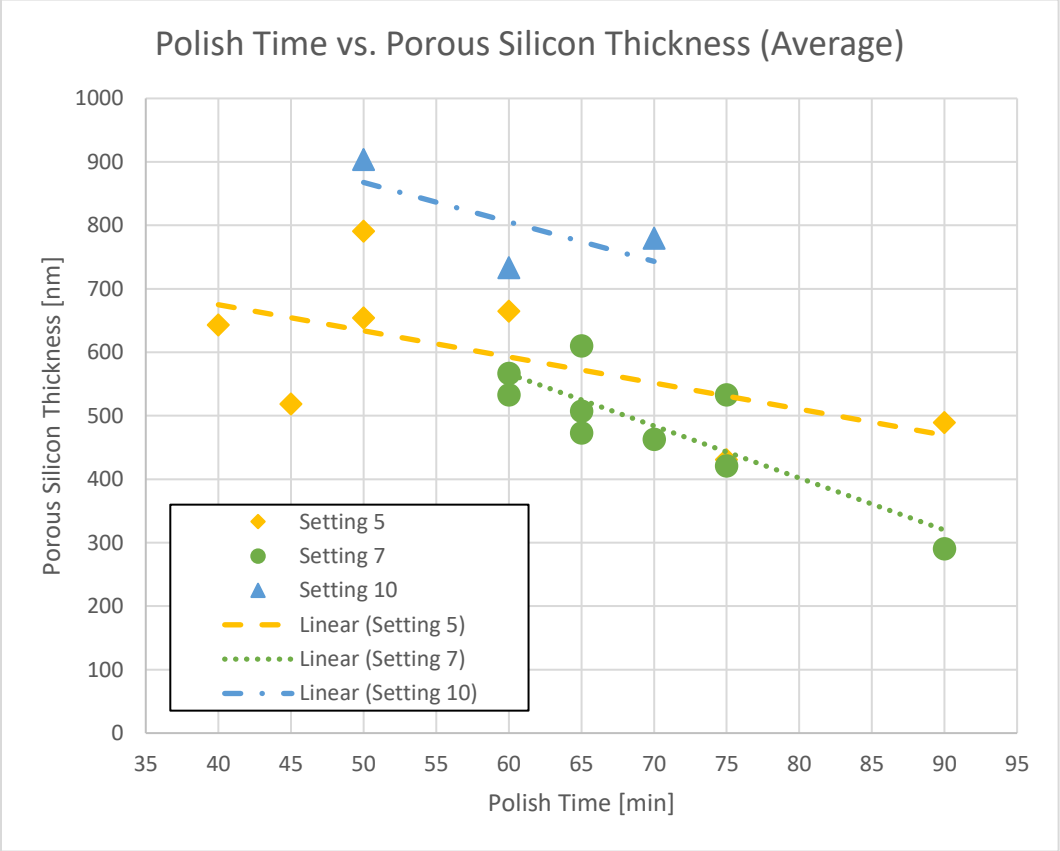

Figure S24. A graph showing final polished thickness vs. polish time for three different polishing settings; setting 5 indicates 5% amplitude, setting 7 indicates 70% amplitude, and setting 10 indicates 100% amplitude

REFERENCES

[1] A. Vijayakumar and S. Bhattacharya, *Design and Fabrication of Diffractive Optical Elements with MATLAB*, vol. TT109. SPIE Press, 2017.

[2] F. Capasso, “The future and promise of flat optics: a personal perspective,” *Nanophotonics*, vol. 7, no. 6, pp. 953–957, Jun. 2018, doi: 10.1515/nanoph-2018-0004.

[3] J. Nelson, F. Nürnberg, B. Kühn, R. Jedamzik, U. Petzold, and G. von der Goenna, *Review of Optical Manufacturing 2000 to 2020*. SPIE, 2021. doi: 10.1117/3.2599940.

[4] S. Banerji, M. Meem, A. Majumder, F. G. Vasquez, B. Sensale-Rodriguez, and R. Menon, “Imaging with flat optics: metalenses or diffractive lenses?,” *Optica*, vol. 6, no. 6, p. 805, Jun. 2019, doi: 10.1364/OPTICA.6.000805.

[5] M. Ye *et al.*, “Subwavelength Grating Lens With Continuous Phase Shifts,” *IEEE Photonics Technology Letters*, vol. 33, no. 16, pp. 844–847, Aug. 2021, doi: 10.1109/LPT.2021.3076289.

[6] J. M. Luque-González *et al.*, “A review of silicon subwavelength gratings: building break-through devices with anisotropic metamaterials,” *Nanophotonics*, vol. 10, no. 11, pp. 2765–2797, Aug. 2021, doi: 10.1515/nanoph-2021-0110.

[7] S. S. Bukhari, J. Vardaxoglou, and W. Whittow, “A Metasurfaces Review: Definitions and Applications,” *Applied Sciences*, vol. 9, no. 13, p. 2727, Jul. 2019, doi: 10.3390/app9132727.

[8] J. A. Davison and M. J. Simpson, “History and development of the apodized diffractive intraocular lens,” *Journal of Cataract and Refractive Surgery*, vol. 32, no. 5, pp. 849–858, May 2006, doi: 10.1016/j.jcrs.2006.02.006.

[9] A. Motogaito and K. Hiramatsu, “Fabrication of Binary Diffractive Lenses and the Application to LED Lighting for Controlling Luminosity Distribution,” *Optics and Photonics Journal*, vol. 03, no. 01, pp. 67–73, 2013, doi: 10.4236/opj.2013.31011.

[10] P. Wang, N. Mohammad, and R. Menon, “Chromatic-aberration-corrected diffractive lenses for ultra-broadband focusing,” *Scientific Reports*, vol. 6, no. 1, p. 21545, Aug. 2016, doi: 10.1038/srep21545.

[11] M. B. Fleming and M. C. Hutley, “Blazed diffractive optics,” *Applied Optics*, vol. 36, no. 20, p. 4635, Jul. 1997, doi: 10.1364/AO.36.004635.

[12] D. Faklis and G. M. Morris, “Spectral properties of multiorder diffractive lenses,” *Applied Optics*, vol. 34, no. 14, p. 2462, May 1995, doi: 10.1364/AO.34.002462.

[13] D. W. Sweeney and G. E. Sommargren, “Harmonic diffractive lenses,” *Applied Optics*, vol. 34, no. 14, p. 2469, May 1995, doi: 10.1364/AO.34.002469.

[14] N. Mohammad, M. Meem, B. Shen, P. Wang, and R. Menon, “Broadband imaging with one planar diffractive lens,” *Scientific Reports*, vol. 8, no. 1, p. 2799, Dec. 2018, doi: 10.1038/s41598-018-21169-4.

[15] S. Kasap and R. Sinha, *Optoelectronics and Photonics: Principles and Practices*, 2nd ed. Essex: Pearson Education Limited, 2013.

[16] W. Cai and V. Shalaev, *Optical Metamaterials*. New York, NY: Springer New York, 2010. doi: 10.1007/978-1-4419-1151-3.

[17] D. R. Smith, W. J. Padilla, D. C. Vier, S. C. Nemat-Nasser, and S. Schultz, “Composite Medium with Simultaneously Negative Permeability and Permittivity,” *Physical Review Letters*, vol. 84, no. 18, pp. 4184–4187, May 2000, doi: 10.1103/PhysRevLett.84.4184.

[18] R. A. Shelby, D. R. Smith, and S. Schultz, “Experimental Verification of a Negative Index of Refraction,” *Science (1979)*, vol. 292, no. 5514, pp. 77–79, Apr. 2001, doi: 10.1126/science.1058847.

[19] V.-C. Su, C. H. Chu, G. Sun, and D. P. Tsai, “Advances in optical metasurfaces: fabrication and applications [Invited],” *Optics Express*, vol. 26, no. 10, p. 13148, May 2018, doi: 10.1364/OE.26.013148.

[20] N. Yu *et al.*, “Light Propagation with Phase Discontinuities: Generalized Laws of Reflection and Refraction,” *Science (1979)*, vol. 334, no. 6054, pp. 333–337, Oct. 2011, doi: 10.1126/science.1210713.

[21] A. Y. Zhu, A. I. Kuznetsov, B. Luk’yanchuk, N. Engheta, and P. Genevet, “Traditional and emerging materials for optical metasurfaces,” *Nanophotonics*, vol. 6, no. 2, pp. 452–471, Mar. 2017, doi: 10.1515/nanoph-2016-0032.

[22] N. Meinzer, W. L. Barnes, and I. R. Hooper, “Plasmonic meta-atoms and metasurfaces,” *Nature Photonics*, vol. 8, no. 12, pp. 889–898, Dec. 2014, doi: 10.1038/nphoton.2014.247.

[23] Nanfang Yu *et al.*, “Flat Optics: Controlling Wavefronts With Optical Antenna Metasurfaces,” *IEEE Journal of Selected Topics in Quantum Electronics*, vol. 19, no. 3, pp. 4700423–4700423, May 2013, doi: 10.1109/JSTQE.2013.2241399.

[24] A. Pors, M. G. Nielsen, R. L. Eriksen, and S. I. Bozhevolnyi, “Broadband Focusing Flat Mirrors Based on Plasmonic Gradient Metasurfaces,” *Nano Letters*, vol. 13, no. 2, pp. 829–834, Feb. 2013, doi: 10.1021/nl304761m.

[25] M. Chen, M. Kim, A. M. H. Wong, and G. v. Eleftheriades, “Huygens’ metasurfaces from microwaves to optics: a review,” *Nanophotonics*, vol. 7, no. 6, pp. 1207–1231, Jun. 2018, doi: 10.1515/nanoph-2017-0117.

[26] C. Pfeiffer, N. K. Emani, A. M. Shaltout, A. Boltasseva, V. M. Shalaev, and A. Grbic, “Efficient Light Bending with Isotropic Metamaterial Huygens’ Surfaces,” *Nano Letters*, vol. 14, no. 5, pp. 2491–2497, May 2014, doi: 10.1021/nl5001746.

[27] A. Arbabi, Y. Horie, M. Bagheri, and A. Faraon, "Dielectric metasurfaces for complete control of phase and polarization with subwavelength spatial resolution and high transmission," *Nature Nanotechnology*, vol. 10, no. 11, pp. 937–943, Nov. 2015, doi: 10.1038/nnano.2015.186.

[28] J. M. Luque-González *et al.*, "An Ultracompact GRIN-Lens-Based Spot Size Converter using Subwavelength Grating Metamaterials," *Laser & Photonics Reviews*, vol. 13, no. 11, p. 1900172, Nov. 2019, doi: 10.1002/lpor.201900172.

[29] J. M. Luque-González *et al.*, "Tilted subwavelength gratings: controlling anisotropy in metamaterial nanophotonic waveguides," *Optics Letters*, vol. 43, no. 19, p. 4691, Oct. 2018, doi: 10.1364/OL.43.004691.

[30] R. Halir *et al.*, "Subwavelength-Grating Metamaterial Structures for Silicon Photonic Devices," *Proceedings of the IEEE*, vol. 106, no. 12, pp. 2144–2157, Dec. 2018, doi: 10.1109/JPROC.2018.2851614.

[31] R. Halir *et al.*, "Colorless directional coupler with dispersion engineered sub-wavelength structure," *Optics Express*, vol. 20, no. 12, p. 13470, Jun. 2012, doi: 10.1364/OE.20.013470.

[32] Y. Wang *et al.*, "Compact Broadband Directional Couplers Using Subwavelength Gratings," *IEEE Photonics Journal*, vol. 8, no. 3, pp. 1–8, Jun. 2016, doi: 10.1109/JPHOT.2016.2574335.

[33] L. Xu *et al.*, "Compact high-performance adiabatic 3-dB coupler enabled by subwavelength grating slot in the silicon-on-insulator platform," *Optics Express*, vol. 26, no. 23, p. 29873, Nov. 2018, doi: 10.1364/OE.26.029873.

[34] H. Yun, L. Chrostowski, and N. A. F. Jaeger, "Ultra-broadband 2 × 2 adiabatic 3 dB coupler using subwavelength-grating-assisted silicon-on-insulator strip waveguides," *Optics Letters*, vol. 43, no. 8, p. 1935, Apr. 2018, doi: 10.1364/OL.43.001935.

[35] A. Ortega-Moñux *et al.*, "An ultra-compact multimode interference coupler with a subwavelength grating slot," *Laser & Photonics Reviews*, vol. 7, no. 2, pp. L12–L15, Mar. 2013, doi: 10.1002/lpor.201200106.

[36] W. Zhong and J. Xiao, "Ultracompact polarization-insensitive power splitter using subwavelength-grating-based MMI couplers on an SOI platform," *Applied Optics*, vol. 59, no. 7, p. 1991, Mar. 2020, doi: 10.1364/AO.382097.

[37] N. L. Kazanskiy, M. A. Butt, and S. N. Khonina, "Silicon photonic devices realized on refractive index engineered subwavelength grating waveguides-A review," *Optics & Laser Technology*, vol. 138, p. 106863, Jun. 2021, doi: 10.1016/j.optlastec.2020.106863.

[38] J. Gonzalo Wangüemert-Pérez *et al.*, "Evanescent field waveguide sensing with subwavelength grating structures in silicon-on-insulator," *Optics Letters*, vol. 39, no. 15, p. 4442, Aug. 2014, doi: 10.1364/OL.39.004442.

[39] P. Xu, J. Zheng, J. Zhou, Y. Chen, C. Zou, and A. Majumdar, “Multi-slot photonic crystal cavities for high-sensitivity refractive index sensing,” *Optics Express*, vol. 27, no. 3, p. 3609, Feb. 2019, doi: 10.1364/OE.27.003609.

[40] V. Donzella, A. Sherwali, J. Flueckiger, S. M. Grist, S. T. Fard, and L. Chrostowski, “Design and fabrication of SOI micro-ring resonators based on sub-wavelength grating waveguides,” *Optics Express*, vol. 23, no. 4, p. 4791, Feb. 2015, doi: 10.1364/OE.23.004791.

[41] J. Flueckiger *et al.*, “Sub-wavelength grating for enhanced ring resonator biosensor,” *Optics Express*, vol. 24, no. 14, p. 15672, Jul. 2016, doi: 10.1364/OE.24.015672.

[42] D. M. Kita, J. Michon, S. G. Johnson, and J. Hu, “Are slot and sub-wavelength grating waveguides better than strip waveguides for sensing?,” *Optica*, vol. 5, no. 9, p. 1046, Sep. 2018, doi: 10.1364/OPTICA.5.001046.

[43] P. Cheben, D.-X. Xu, S. Janz, and A. Densmore, “Subwavelength waveguide grating for mode conversion and light coupling in integrated optics,” *Optics Express*, vol. 14, no. 11, p. 4695, 2006, doi: 10.1364/OE.14.004695.

[44] P. Cheben *et al.*, “Broadband polarization independent nanophotonic coupler for silicon waveguides with ultra-high efficiency,” *Optics Express*, vol. 23, no. 17, p. 22553, Aug. 2015, doi: 10.1364/OE.23.022553.

[45] R. Halir, P. Cheben, S. Janz, D.-X. Xu, Í. Molina-Fernández, and J. G. Wangüemert-Pérez, “Waveguide grating coupler with subwavelength microstructures,” *Optics Letters*, vol. 34, no. 9, p. 1408, May 2009, doi: 10.1364/OL.34.001408.

[46] Y. Wang *et al.*, “Design of broadband subwavelength grating couplers with low back reflection,” *Optics Letters*, vol. 40, no. 20, p. 4647, Oct. 2015, doi: 10.1364/OL.40.004647.

[47] X. Chen and H. K. Tsang, “Polarization-independent grating couplers for silicon-on-insulator nanophotonic waveguides,” *Optics Letters*, vol. 36, no. 6, p. 796, Mar. 2011, doi: 10.1364/OL.36.000796.

[48] M. Gharghi *et al.*, “A Carpet Cloak for Visible Light,” *Nano Letters*, vol. 11, no. 7, pp. 2825–2828, Jul. 2011, doi: 10.1021/nl201189z.

[49] M. Ye, V. Ray, and Y. S. Yi, “Achromatic Flat Subwavelength Grating Lens Over Whole Visible Bandwidths,” *IEEE Photonics Technology Letters*, vol. 30, no. 10, pp. 955–958, May 2018, doi: 10.1109/LPT.2018.2825198.

[50] P. Cheben, R. Halir, J. H. Schmid, H. A. Atwater, and D. R. Smith, “Subwavelength integrated photonics,” *Nature*, vol. 560, no. 7720, pp. 565–572, Aug. 2018, doi: 10.1038/s41586-018-0421-7.

[51] A. A. Tseng, Kuan Chen, C. D. Chen, and K. J. Ma, “Electron beam lithography in nanoscale fabrication: recent development,” *IEEE Transactions on Electronics Packaging Manufacturing*, vol. 26, no. 2, pp. 141–149, Apr. 2003, doi: 10.1109/TEPM.2003.817714.

[52] Beckers, Ven, Horst, Astakhov, and Banine, “EUV-Induced Plasma: A Peculiar Phenomenon of a Modern Lithographic Technology,” *Applied Sciences*, vol. 9, no. 14, p. 2827, Jul. 2019, doi: 10.3390/app9142827.

[53] C. Fourmentin *et al.*, “IR GRIN lenses prepared by ionic exchange in chalcohalide glasses,” *Scientific Reports*, vol. 11, no. 1, p. 11081, Dec. 2021, doi: 10.1038/s41598-021-90626-4.

[54] O. M. Efimov, L. B. Glebov, L. N. Glebova, K. C. Richardson, and V. I. Smirnov, “High-efficiency Bragg gratings in photothermorefractive glass,” *Applied Optics*, vol. 38, no. 4, p. 619, Feb. 1999, doi: 10.1364/AO.38.000619.

[55] S. Bachevillier *et al.*, “Planar refractive index patterning through microcontact photo-thermal annealing of a printable organic/inorganic hybrid material,” *Materials Horizons*, vol. 9, no. 1, pp. 411–416, 2022, doi: 10.1039/D1MH01366A.

[56] S. Novak *et al.*, “Direct Electrospray Printing of Gradient Refractive Index Chalcogenide Glass Films,” *ACS Applied Materials & Interfaces*, vol. 9, no. 32, pp. 26990–26995, Aug. 2017, doi: 10.1021/acsami.7b06140.

[57] D. Werdehausen *et al.*, “Design rules for customizable optical materials based on nanocomposites,” *Optical Materials Express*, vol. 8, no. 11, p. 3456, Nov. 2018, doi: 10.1364/OME.8.003456.

[58] H. Sohn, “Refractive index of Porous Silicon,” in *Handbook of Porous Silicon*, 1st ed., vol. 1, L. Canham, Ed. Cham: Springer International Publishing, 2018. doi: 10.1007/978-3-319-71381-6.

[59] R. Valiullin, “Mesoporous Silicon,” in *Handbook of Porous Silicon*, 1st ed., vol. 1, L. Canham, Ed. Cham: Springer International Publishing, 2018. doi: 10.1007/978-3-319-71381-6.

[60] T. H. Talukdar, J. C. Perez, and J. D. Ryckman, “Nanoimprinting of Refractive Index: Patterning Subwavelength Effective Media for Flat Optics,” *ACS Applied Nano Materials*, vol. 3, no. 8, pp. 7377–7383, Aug. 2020, doi: 10.1021/acsanm.0c01395.

[61] E. Pérez, “Fundamentals of porous silicon and applications,” Rovira i Virgili University, Tarragona, 2006.

[62] L. Canham, “Porous Silicon Application Survey,” in *Handbook of Porous Silicon*, 1st ed., vol. 2, L. Canham, Ed. Cham: Springer International Publishing, 2018. doi: 10.1007/978-3-319-71381-6.

[63] A. Loni, “Porous Silicon Formation by Anodization,” in *Handbook of Porous Silicon*, 1st ed., vol. 1, L. Canham, Ed. Cham: Springer International Publishing, 2018. doi: 10.1007/978-3-319-71381-6.

[64] M. Sailor, *Porous Silicon in Practice: Preparation, Characterization and Applications*, Illustrated. John Wiley & Sons, 2012.

[65] R. Herino, G. Bomchil, K. Barla, C. Bertrand, and J. L. Ginoux, “Porosity and Pore Size Distributions of Porous Silicon Layers,” *Journal of The Electrochemical Society*, vol. 134, no. 8, pp. 1994–2000, Aug. 1987, doi: 10.1149/1.2100805.

[66] L. Canham, “Mechanical Properties of Porous Silicon,” in *Handbook of Porous Silicon*, 1st ed., vol. 1, L. Canham, Ed. Cham: Springer International Publishing, 2018. doi: 10.1007/978-3-319-71381-6.

[67] E. V. Astrova and V. A. Tolmachev, “Effective refractive index and composition of oxidized porous silicon films,” *Materials Science and Engineering: B*, vol. 69–70, pp. 142–148, Jan. 2000, doi: 10.1016/S0921-5107(99)00236-6.

[68] L. Canham, “Tunable Properties of Porous Silicon,” in *Handbook of Porous Silicon*, 1st ed., vol. 1, L. Canham, Ed. Cham: Springer International Publishing, 2018. doi: 10.1007/978-3-319-71381-6.

[69] S. P. Duttagupta, X. L. Chen, S. A. Jenekhe, and P. M. Fauchet, “Microhardness of porous silicon films and composites,” *Solid State Communications*, vol. 101, no. 1, pp. 33–37, Jan. 1997, doi: 10.1016/S0038-1098(96)00546-7.

[70] Ch. Populaire, B. Remaki, V. Lysenko, D. Barbier, H. Artmann, and T. Pannek, “On mechanical properties of nanostructured meso-porous silicon,” *Applied Physics Letters*, vol. 83, no. 7, pp. 1370–1372, Aug. 2003, doi: 10.1063/1.1603336.

[71] M. Fujii and J. Diener, “Optical Birefringence of Porous silicon,” in *Handbook of Porous Silicon*, 1st ed., vol. 1, L. Canham, Ed. Cham: Springer International Publishing, 2018. doi: 10.1007/978-3-319-71381-6.

[72] A. E. Pap *et al.*, “Optical properties of porous silicon. Part III: Comparison of experimental and theoretical results,” *Opt Mater (Amst)*, vol. 28, no. 5, pp. 506–513, Apr. 2006, doi: 10.1016/j.optmat.2005.02.006.

[73] M. Khardani, M. Bouaïcha, and B. Bessaïs, “Bruggeman effective medium approach for modelling optical properties of porous silicon: comparison with experiment,” *physica status solidi c*, vol. 4, no. 6, pp. 1986–1990, May 2007, doi: 10.1002/pssc.200674420.

[74] S. Ram, “Electrical Transport in Porous Silicon,” in *Handbook of Porous Silicon*, 1st ed., vol. 1, L. Canham, Ed. Cham: Springer International Publishing, 2018. doi: 10.1007/978-3-319-71381-6.

[75] S. Low and N. Voelcker, “Biocompatibility of Porous Silicon,” in *Handbook of Porous Silicon*, 1st ed., vol. 1, L. Canham, Ed. Cham: Springer International Publishing, 2018. doi: 10.1007/978-3-319-71381-6.

[76] M. Sailor, “Chemical Reactivity and Surface chemistry of porous silicon,” in *Handbook of Porous Silicon*, 1st ed., vol. 1, L. Canham, Ed. Cham: Springer International Publishing, 2018. doi: 10.1007/978-3-319-71381-6.

[77] B. Gupta, Y. Zhu, B. Guan, P. J. Reece, and J. J. Gooding, “Functionalised porous silicon as a biosensor: emphasis on monitoring cells in vivo and in vitro,” *Analyst*, vol. 138, no. 13, p. 3593, 2013, doi: 10.1039/c3an00081h.

[78] B. P. Azeredo, Y. Lin, A. Avagyan, M. Sivaguru, K. Hsu, and P. Ferreira, “Direct Imprinting of Porous Silicon via Metal-Assisted Chemical Etching,” *Advanced Functional Materials*, vol. 26, no. 17, pp. 2929–2939, May 2016, doi: 10.1002/adfm.201505153.

[79] A. Keating, “Photolithography on Porous Silicon,” in *Handbook of Porous Silicon*, 1st ed., vol. 2, L. Canham, Ed. Cham: Springer International Publishing, 2018. doi: 10.1007/978-3-319-71381-6.

[80] M. Breese, “Ion beam based patterning of porous silicon,” in *Handbook of Porous Silicon*, 1st ed., vol. 2, L. Canham, Ed. Cham: Springer International Publishing, 2018. doi: 10.1007/978-3-319-71381-6.

[81] D. J. Sirbuly, G. M. Lowman, B. Scott, G. D. Stucky, and S. K. Buratto, “Patterned Microstructures of Porous Silicon by Dry-Removal Soft Lithography,” *Advanced Materials*, vol. 15, no. 2, pp. 149–152, Jan. 2003, doi: 10.1002/adma.200390031.

[82] J. D. Ryckman, M. Liscidini, J. E. Sipe, and S. M. Weiss, “Direct Imprinting of Porous Substrates: A Rapid and Low-Cost Approach for Patterning Porous Nanomaterials,” *Nano Letters*, vol. 11, no. 5, pp. 1857–1862, May 2011, doi: 10.1021/nl1028073.

[83] J. Ryckman and S. Weiss, “Imprinting Porous Silicon,” in *Handbook of Porous Silicon*, 1st ed., vol. 2, L. Canham, Ed. Cham: Springer International Publishing, 2018. doi: 10.1007/978-3-319-71381-6.

[84] J. D. Ryckman, Y. Jiao, and S. M. Weiss, “Three-dimensional patterning and morphological control of porous nanomaterials by gray-scale direct imprinting,” *Scientific Reports*, vol. 3, no. 1, p. 1502, Dec. 2013, doi: 10.1038/srep01502.

[85] N. A. Krueger *et al.*, “Electrochemical Fabrication of Flat, Polymer-Embedded Porous Silicon 1D Gradient Refractive Index Microlens Arrays,” *physica status solidi (a)*, vol. 215, no. 13, p. 1800088, Jul. 2018, doi: 10.1002/pssa.201800088.

[86] C. R. Ocier *et al.*, “Optically anisotropic porous silicon microlenses with tunable refractive indexes and birefringence profiles,” *Optical Materials Express*, vol. 10, no. 4, p. 868, Apr. 2020, doi: 10.1364/OME.385013.

[87] N. A. Krueger *et al.*, “Porous Silicon Gradient Refractive Index Micro-Optics,” *Nano Letters*, vol. 16, no. 12, pp. 7402–7407, Dec. 2016, doi: 10.1021/acs.nanolett.6b02939.

[88] S. Ilyas and M. Gal, “Optical devices from porous silicon having continuously varying refractive index,” *Journal of Materials Science: Materials in Electronics*, vol. 18, no. S1, pp. 61–64, Oct. 2007, doi: 10.1007/s10854-007-9174-z.

[89] S. Ilyas and M. Gal, “Gradient refractive index planar microlens in Si using porous silicon,” *Applied Physics Letters*, vol. 89, no. 21, p. 211123, Nov. 2006, doi: 10.1063/1.2396929.

[90] Y. Li *et al.*, “Three-dimensional Ultrathin Planar Lenses by Acoustic Metamaterials,” *Scientific Reports*, vol. 4, no. 1, p. 6830, May 2015, doi: 10.1038/srep06830.

[91] G. A. Rodriguez, S. Hu, and S. M. Weiss, “Porous silicon ring resonator for compact, high sensitivity biosensing applications,” *Optics Express*, vol. 23, no. 6, p. 7111, Mar. 2015, doi: 10.1364/OE.23.007111.

[92] T. H. Talukdar, G. D. Allen, I. Kravchenko, and J. D. Ryckman, “Single-mode porous silicon waveguide interferometers with unity confinement factors for ultra-sensitive surface adlayer sensing,” *Optics Express*, vol. 27, no. 16, p. 22485, Aug. 2019, doi: 10.1364/OE.27.022485.

[93] M. Nedeljkovic, R. Soref, and G. Z. Mashanovich, “Free-Carrier Electrorefraction and Electroabsorption Modulation Predictions for Silicon Over the 1-14 μm infrared wavelength range,” *IEEE Photonics Journal*, vol. 3, no. 6, pp. 1171–1180, Dec. 2011, doi: 10.1109/JPHOT.2011.2171930.

[94] P. Pirasteh, J. Charrier, Y. Dumeige, S. Haesaert, and P. Joubert, “Optical loss study of porous silicon and oxidized porous silicon planar waveguides,” *Journal of Applied Physics*, vol. 101, no. 8, p. 083110, Apr. 2007, doi: 10.1063/1.2718886.

[95] K. Hakshur and S. Ruschin, “Observation of a large optical birefringence effect in a (110) oriented porous silicon layer,” *Applied Physics Letters*, vol. 104, no. 5, p. 051909, Feb. 2014, doi: 10.1063/1.4863746.